China Geology 6 (2023) 623−645

China Geology

Journal homepage: http://chinageology.cgs.cn
https://www.sciencedirect.com/journal/china-geology

Melt extraction and mineralization: A case study from the Shuangjianzishan supergiant Ag-Pb-Zn deposit (208 Mt), Inner Mongolia, NE China

Meng Dai[a], Guang-sheng Yan[b], Yong-sheng Li[c,*], Wen-bin Jia[b], Fan-yu Qi[c,*], Xing Ju[a]

[a] *China Aero Geophysical and Remote Sensing Center for Natural Resources*, *China Geology Survey*, *Ministry of Natural Resources*, *Beijing* 100083, *China*
[b] *Chinese Academy of Geological Sciences*, *China Geology Survey*, *Ministry of Natural Resources*, *Beijing* 100037, *China*
[c] *Development and Research Center*, *China Geology Survey*, *Ministry of Natural Resources*, *Beijing* 100037, *China*

ARTICLE INFO

Article history:
Received 25 January 2022
Received in revised form 9 July 2022
Accepted 19 July 2022
Available online 18 October 2022

Keywords:
Ag-Pb-Zn deposit
D-O-C-He-Ar isotope
In-situ S and Pb isotope analysis
Melt extraction
Ore-forming fluid
Syenogranite
Metallogenic belt
Mineral exploration engineering
Southern Great Hinggan Range

ABSTRACT

The supergiant Shuangjianzishan (SJZ) Ag-Pb-Zn deposit is in the southern segment of the Great Hinggan Range (SGHR), northeast China. Previous studies suggest the ore-forming material and fluid originated from the magmatic system, and the mineralization age was consistent with the diagenetic age. However, the relationship between granitic magmatism and mineralization is still unclear in the SJZ. In this study, C-H-O-He-Ar and *in-situ* S-Pb isotope analyses were conducted to determine the sources of ore-forming fluids and metals, which were combined with geochemistry data of SJZ granitoids from previous studies to constrain the relationship between the magmatism and the mineralization. The C-H-O-He-Ar-S-Pb isotopic compositions suggested the SJZ ore-forming material and fluids were derived from a magmatic source, which has mixed a small amount of mantle-derived materials. In addition, the disseminated sulfide from the syenogranite has comparable S-Pb isotopic composition with the sulfide minerals from ore veins, suggesting that the generation of the SJZ ore-forming fluids has a close relationship with the syenogranite magmatism. Combining with the geochemical characters of the syenogranite, the authors proposed that the mantle-derived fingerprint of the SJZ ore-forming fluid might be caused by the parent magma of the syenogranite, which was derived from partial melting of the juvenile lower crust, and underwent the residual melts segregated from a crystal mush in the shallow magma reservoir. The extraction of the syenogranite parent magma further concentrated the fertilized fluids, which was crucial to mineralization of the SJZ Ag-Pb-Zn deposit.

1. Introduction

The supergiant Shuangjianzishan (SJZ) Ag-Pb-Zn deposit is located in the southern Great Hinggan Range (SGHR), which reported proven reserves of 161.22×10^6 Mt ore volume, Ag metal content 15.5×10^3 Mt, Pb metal content 392×10^3 Mt, and Zn metal content 392×10^3 Mt (Wang XD et al., 2018). The SJZ Ag-Pb-Zn deposit and other adjacent Cu-Mo-Pb-Zn-Ag deposits constitute one of the most important Cu-Sn-Ag-Pb-Zn polymetals producing regions of China (Shu QH et al., 2013; Jiang SH et al., 2011a, 2011b, 2017; Liu YF et al., 2016a, 2017; Liu LH, 2018; Zhai DG et al., 2017, 2018a; Yang H et al., 2020; Jiang B et al., 2022).

Previous studies pointed out that the SGHR Mesozoic mineralization was triggered by the Mesozoic intensive magmatism, which was caused by the subduction and collisional events of the Mongol-Okhotsk Ocean, and the Paleo-Pacific Ocean (Liu C et al., 2011; Nie FJ et al., 2007; Xiao WJ et al., 2009; Xu B et al., 2015; Jiang SH et al., 2017; Li JY et al., 2021). The ore-bodies of the SJZ Ag-Pb-Zn deposit are hosted around intermediate-acid intrusions emplaced into adjacent terranes, which is the same as other polymetallic deposits (Cu-Mo-Pb-Zn-Ag) in the world (Baker T et al., 2004). The spatial and temporal relationships between intrusions and polymetallic-vein mineralization have been documented in the SJZ Ag-Pb-Zn deposits (Zhai DG et al., 2020; Zhang SH et al, 2019; Dai M et al., 2022). However, these polymetallic veins do not show a genetic relationship to the intrusions in the SJZ Ag-Pb-Zn deposit. In recent years, many studies have been done on the SJZ Ag-Pb-Zn deposit, such as the geological characteristics, ore-forming fluid

First author: *E-mail address*: sdiamond@qq.com (Meng Dai).
* Corresponding author: *E-mail address*: 39220556@qq.com (Yong-sheng Li); 46749690@qq.com (Fan-yu Qi).

Literary editor: Li-qiong Jia
doi:10.31035/cg2022044
2096-5192/© 2023 China Geology Editorial Office.

evolution, and precipitation mechanisms (Cai HA et al., 2021; Liu YF et al., 2016a, 2016b; Zhang HY et al., 2019; Zhai DG et al., 2020; Wang XD et al., 2018). These study results suggest the SJZ ore-forming fluids and ore-forming material originated from a magma source. Zhai DG et al. (2020) pointed out that the ore-forming fluid and its metals were exsolved during the crystallization of the final phase of a composite granite porphyry intrusion. However, the relationship between Early-Cretaceous magmatism and mineralization remains poorly constrained, such as the identification of causative intrusions and the mechanism of concentration for ore-forming elements in the process of magma evolution.

In this study, the authors present new multiple isotope (C, H, He, Ar, S, Pb) data from the ore-bearing quartz/calcite veins and sulfides. Using these data with a combination of available geological and the published lithogeochemistry data of the SJZ intrusive rocks from previous studies, the authors aim to reveal the causative intrusion and the mechanism of concentration for ore-forming elements in the process of magma evolution at the SJZ Ag-Pb-Zn deposit.

2. Regional geology

The SJZ Ag-Pb-Zn deposit is found in the southern SGHR metallogenic belt. The SGHR is in the eastern segment of the Central Asian Orogenic Belt (CAOB), which is surrounded by the Siberian, North China, and Tarim Cratons (Fig. 1a). The major terranes in the SGHR are the Xing ’an-Airgin Sum Block separated by the Erlian–Hegenshan Fault in the north, the Xar Moron Fault in the south, and the Nenjiang Fault in the northeast (Fig. 1b; Ouyang FG et al., 2015; Jiang SJ et al., 2017). Outcropping strata in the southern GHR are Permian and Jurassic volcanic–sedimentary rocks. The Permian terranes consist of the Early Permian Dashizhai, Huanggangliang, and the Late Permian Linxi Formations. The Dashizhai Formation is consisted of a basaltic to granitic shallow submarine volcanic assemblage, which is an important ore bearing strata (Nie FJ et al., 2007; Niu SY et al., 2008). The Late Jurassic strata is consisted of rhyolite and intermediate-acid pyroclastics (Nie FJ et al., 2007).

The Mesozoic tectonic history of the SGHR is complex, involving the final closure of the Paleo-Asian Ocean in the Late Paleozoic–Early Mesozoic, the closure of the Mongol-Okhotsk Ocean in the Early Mesozoic, and the westward advance of the Paleo-Pacific plate in the Late Mesozoic (Sengör AMC and Natal’in BA., 1996; Xiao WJ et al., 2009; Xu B et al., 2015; Zhou JB and Wild SA, 2013; Ouyang HG et al., 2015). Therefore, the Mesozoic igneous rocks are widely distributed in the SGHR (Wu FY et al., 2011; Xu B et al., 2012; Ouyang HG et al., 2014). Based on previous precise geochronological research on regional intrusion rocks, these volcanic rocks and granitoids can be broadly divided into two episodes that are the Permian–Triassic episode (275 Ma to 210 Ma, zircon U-Pb method) and the Jurassic–Cretaceous episode (160 Ma to 130 Ma, zircon U-Pb method) (Li JF et al., 2016; Wu FY et al. 2004; Zhang JH et al.2010; Wei CS et al., 2017). Previous studies suggested that the Late Mesozoic magmatism of the SGHR was caused by the break-off of the southward subduction of the Mongol-Okhotsk oceanic slab at depth, which led to subsequent lithospheric extension and upwelling asthenosphere (Xu WL et al., 2013; Ouyang HG et al., 2015; Jiang SH et al., 2017). The SGHR hosts many large-scale deposits, e.g., the Weilasituo Cu-Zn-Ag polymetallic vein-type deposit (Liu YF et al., 2016, 2017), the Huanggangliang skarn-type Fe-Sn deposit (Zhai DG et al., 2014), and the Bianjiadayuan Ag-Pb-Zn polymetallic vein-type deposit (Zhai DG et al., 2017). Previous research has suggested that the deposits in this area are mostly related to Late Mesozoic magmatism, and are predominantly associated with NW- and NE-trending normal faults (Mao JW et al., 2005; Zhai DG et al., 2014; Ouyang HG et al., 2015).

3. Ore deposit geology

The Dashizhai, Xinmin, and Manketou'ebo Formations, and unassigned Holocene sediments are observed in the SJZ Ag-Pb-Zn deposit (Fig. 2). Specifically, the Dashizhai Formation consists of grayish-green metamorphic andesite, andesitic tuff, and black argillaceous slate (Fig. 2b); the Xinmin Formation is a sandy conglomerate, siltstone intercalated with carbonaceous mudstone, and thin coal seams that unconformably on the Dashizhai Formation (Figs. 3, 4a); the Manketou ’ebo Formations is consisted of felsic tuff, greywacke, and tuffaceous sandstone. The NW- and NE-trending faults predominate in the SJZ structures, which are contemporaneous structures. The NE- trending faults are generally 50–600 m long and 1–8 m wide, with strikes ranging between 20° and 40° and dips of about 60° NW (Fig, 3). The NW- trending faults are greater than 400 m long, 6–15 m wide, and along their edges occurred many secondary compressive fractures which are filled by quartz/calcite–sulfide veins[①]. The intrusive rocks in the SJZ district are a suite of felsic magmatic rocks, which consist of diorite porphyry, syenogranite, and monzogranite. The granitoids can only be observed in drill cores (ZK1237) in the northwestern ore district (Fig. 4d), which is characterized by the gradual contact relationship between fine-grained syenogranite in the upper and coarse-grained monzogranite in the bottom. Disseminated pyrite, galena, sphalerite, and magnetite mineralizations are developed in the fine-grained syenogranite (Fig. 4). The diorite porphyry dykes are generally 200–800 m long, 10–30 m wide, and generally strike NW, with disseminated pyrite mineralization, vein-type sphalerite, and galena mineralization[②].

[①]Sun KW, Yang SX, Liu YL, Zhang SJ, Zhang LB, Li ZY. 2010. The prospecting report of the Shuangjianzishan Ag-Pb deposit, Balinzuoqi, Inner Mongolia (unpublished technical report). Tiantong geological exploration company., LTD, Chifeng City, Inner Mongolia, 1–96 (in Chinese).

[②]Zheng GR, Zhang SJ, Liu DY. 2015. The supplementary prospecting report of the Shuangjianzishan Ag-Pb deposit, Balinzuoqi, Inner Mongolia (unpublished technical report).Tiantong Geological Exploration Company, Chifeng City, Inner Mongolia, 1–96 (in Chinese).

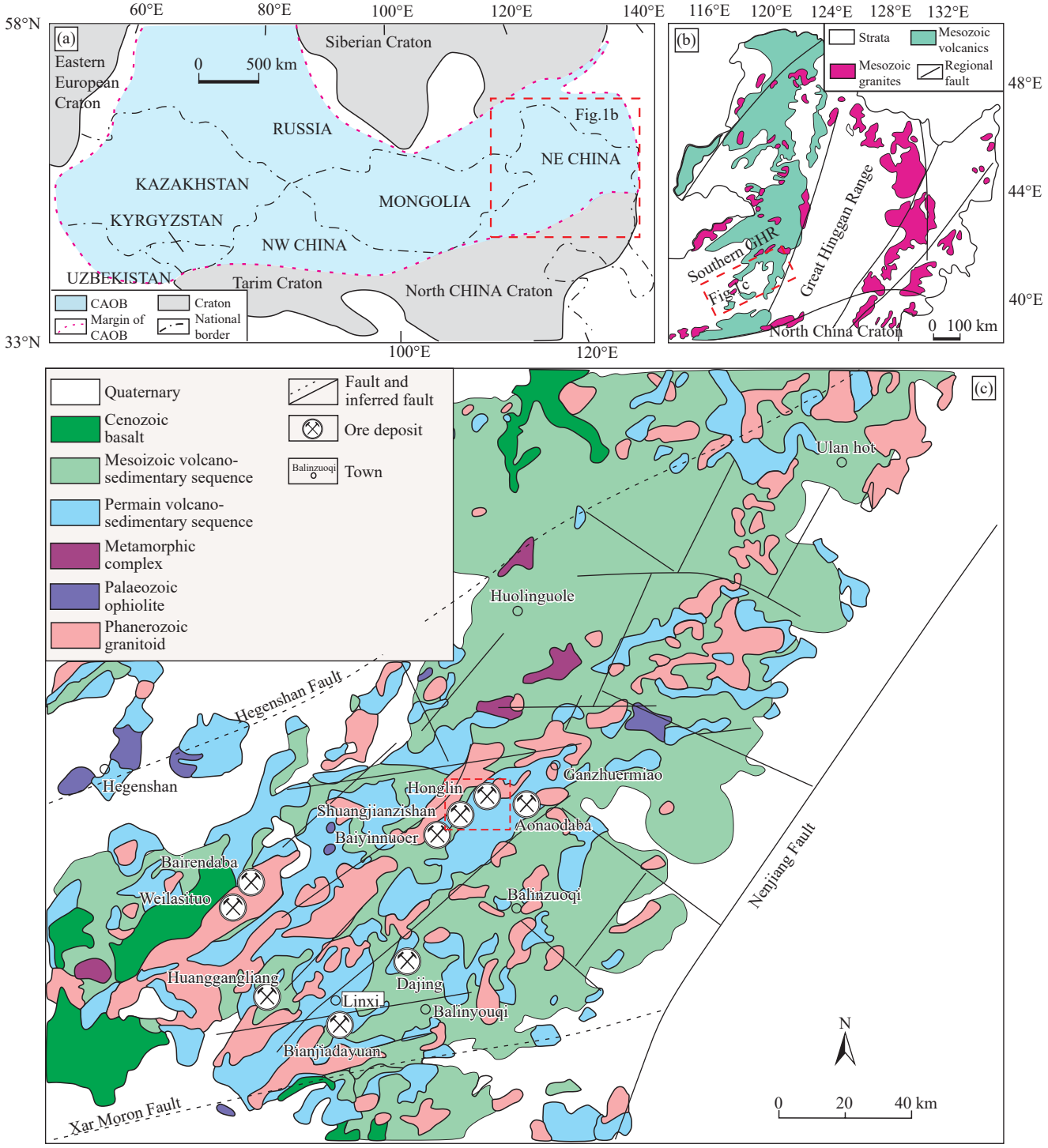

Fig. 1. a–Tectonic scheme of the Central Asian orogenic belt (CAOB, modified from Jahn BM et al., 2000; Shen P et al., 2015); b–geologic map of the Great Hinggan Range (GHR) in northeast China showing the distribution of the Mesozoic granites and volcanic rocks (modified from Zhai DG et al., 2017); c–geologic map of the southern Great Hinggan Range showing the locations and timing of major ore deposits (modified from Ouyang HG et al., 2015).

The host rock is characterized by brecciated with silicification, choritization, epidotization, carbonatization, pyritization, and carbonate alteration (Zhai DG et al., 2019a, 2019b). The silicification has a close relationship with the mineralization, which occurred on both sides of the ore veins (Fig. 5). The ore minerals are native silver, eugenite, argentite, galena, sphalerite, pyrite, chalcopyrite, and marcasite, and they mainly occur in polymetallic quartz veins/veinlets and stockworks or dissemination around these veinlets (Kuang YS et al., 2014). The silver in ores occurs mainly as independent silver minerals (native silver minerals and eugenite) around sulfides or in disulfide cracks (Kuang YS et al., 2014; Zheng GR et al., 2015). Quartz and calcite are the major gangue minerals, along with minor amounts of sericite.

The mineralization is generally massive veins/veinlets and

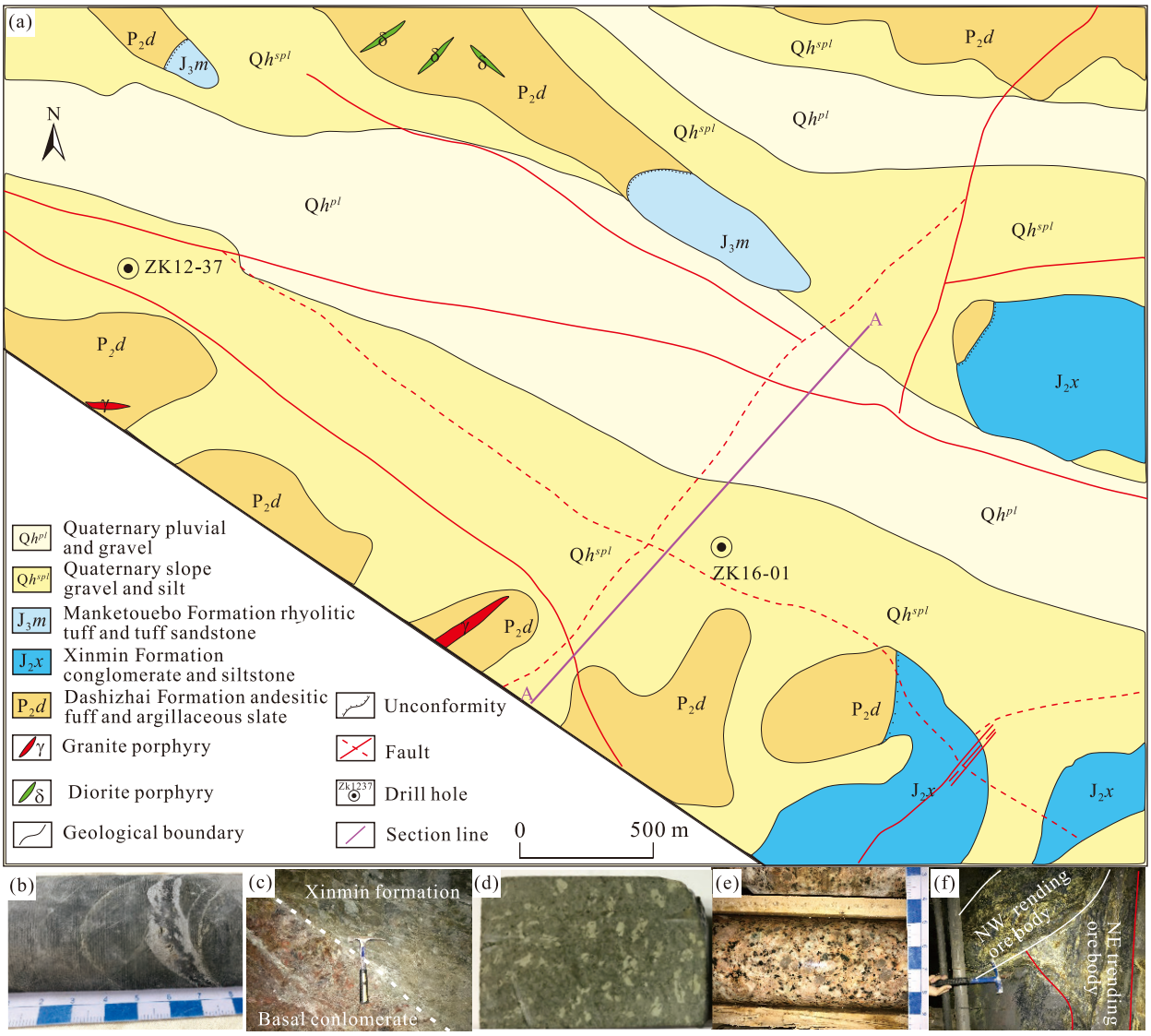

Fig. 2. a–Map of the SJZ Ag-Pb-Zn deposit (modified from Zheng GR et al., 2015①); b–Dashizhai Formation slate; c–unconformity interface between the Xinmin Formation and the Dashizhai Formation; d–coarse-grained porphyritic syenogranite; e–NE- and NW- trending ore bodies.

stockworks or disseminations, with some breccia textures. Sulfides precipitated later than quartz and filled in the vugs and interstices of the quartz, leading to the sulfides forming massive structures in the quartz veins (Fig. 4). Under polarized light, the zonal textures have been observed in the sphalerite crystals, which is charactered by brown coloration in the core and bright yellow at the rim (Fig. 4). Those zonal textures are interpreted to the inhomogeneous composition of the ore-forming fluid during crystallization (Cook NJ et al., 2009; Ye L et al., 2011). The micro-veined and disseminated chalcopyrite was observed in double-crystal joints and cracks of sphalerite (Fig. 4), which have significant differences with vermicular chalcopyrite inclusions in sphalerite (Barton PB and Bethke PM, 1987; Eldridge CS et al., 1988). Thus, these textures were generated by replacement, but exsolution. The silver minerals occur as intergrowths with galena and sphalerite (Fig. 4).

Three stages of the mineralization in the SJZ have been identified by the extensive observation of the mineralogical associations and mineral structure, which consists of the early-, main-, and late-ore stages. In the early-ore stage, euhedral pyrite (1–5 mm) formed in the roof of the ore bodies. In the main-ore stage, a complex polymetallic sulfide assemblage cocrystaled with quartz and calcite, and these sulfides are composed of black sphalerite, galena, silver minerals, and pyrite, which are characterized by coarse-grained and subhedral–euhedral textures (Fig. 5). Sulfides infilled the residual vuggy porosity of earlier quartz generations, which resulted in the veins typically displaying drusy crystal growth and similar encrustations (Fig. 5e). The late-ore stage is represented by fine-grained xenomorphic pyrite (0.01–0.10 mm), which occurs at the wall rock near the ore bodies (Fig. 5f).

①Zheng GR, Zhang SJ, Liu DY. 2015. The supplementary prospecting report of the Shuangjianzishan Ag-Pb deposit, Balinzuoqi, Inner Mongolia (unpublished technical report).Tiantong Geological Exploration Company, Chifeng City, Inner Mongolia, 1–96 (in Chinese).

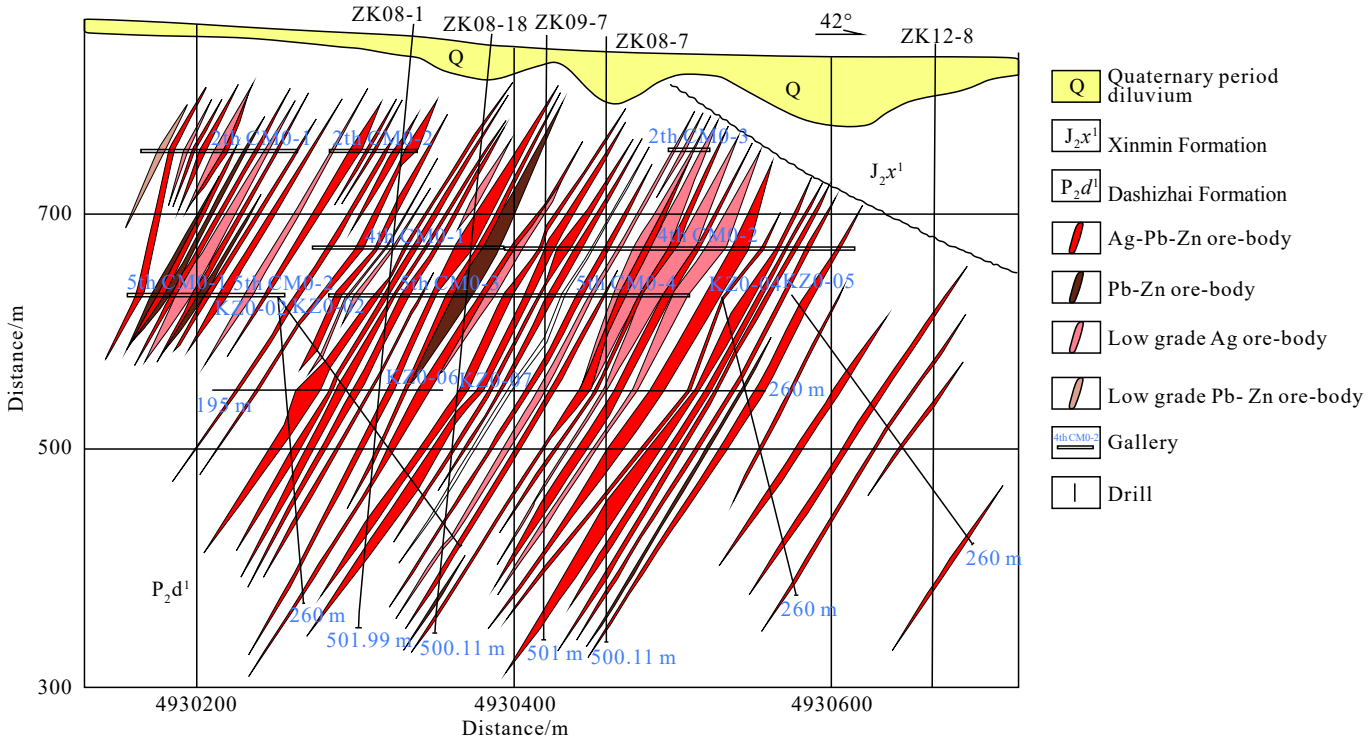

Fig. 3. Prospecting line profile map of the SJZ Ag-Pb-Zn deposit (after Cai HA et al., 2021; Wang XD et al., 2018).

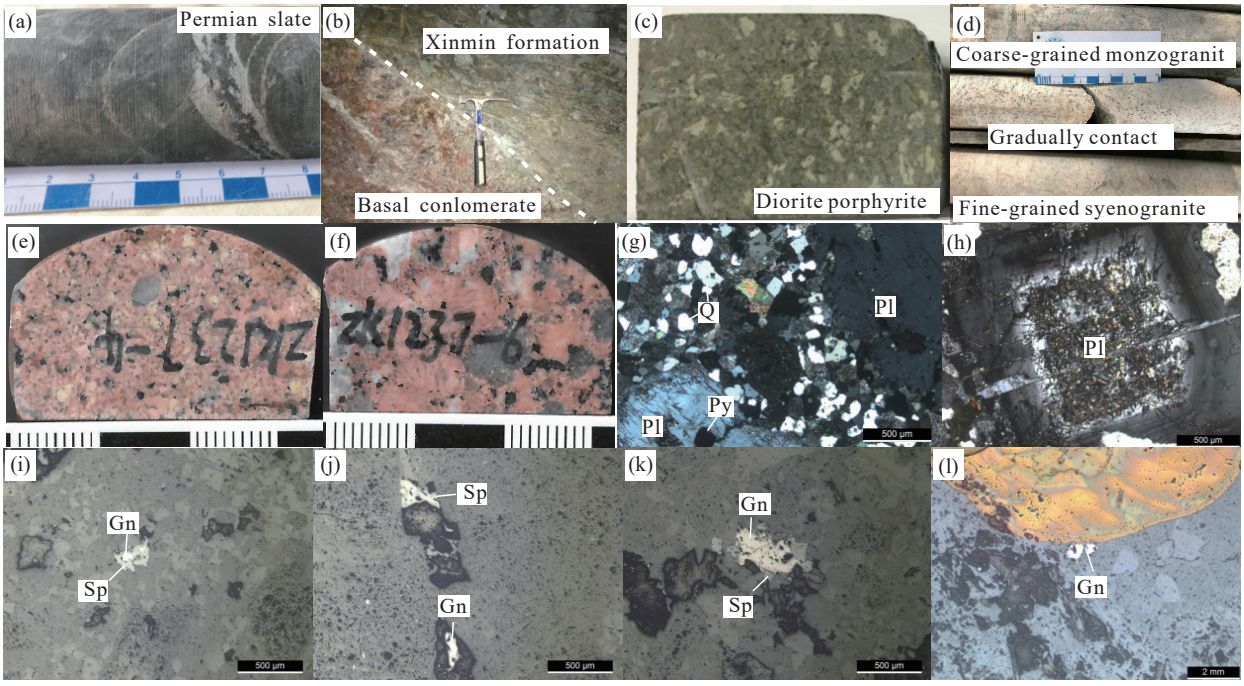

Fig. 4. Representative rock samples from SJZ Ag-Pb-Zn deposit. a–Permian slate; b–Xinmin Formation (Jurassic dacite lava and rhyolitic tuff); c–diorite porphyrite; d–the contact relationship between the syenogranite and monzogranite; e–fine-grained syenogranite; f–coarse-grained monzogranite; g–Photomicrographs (in cross-polarized light) of the fine-grained syenogranite; h–plagioclase oscillatory zones in the coarse-grained monzogranite; i–l–micrograph of disseminated sulfides in the syenogranite. Pl–plagioclase; Q–quartze; Py–pyrite; Sp–sphalerite; Gn–galena. Fig. 4d–f are modified from Dai M et al., 2022 .

4. Samples and analytical methods

4.1. C, H, and O isotope analysis

The quartz samples collected from ore-bearing quartz–calcite veins/veinlets were crushed to about 60 mesh powders for hydrogen and oxygen isotope analyses, which were conducted at the Beijing Research Institute of Uranium Geology, Beijing. The measurements were performed using a Finnigan MAT253-type mass spectrometer following the methods used by Clayton, RN, and Mayeda, TK (1963). Oxygen gas was produced by reacting the samples with BrF_5

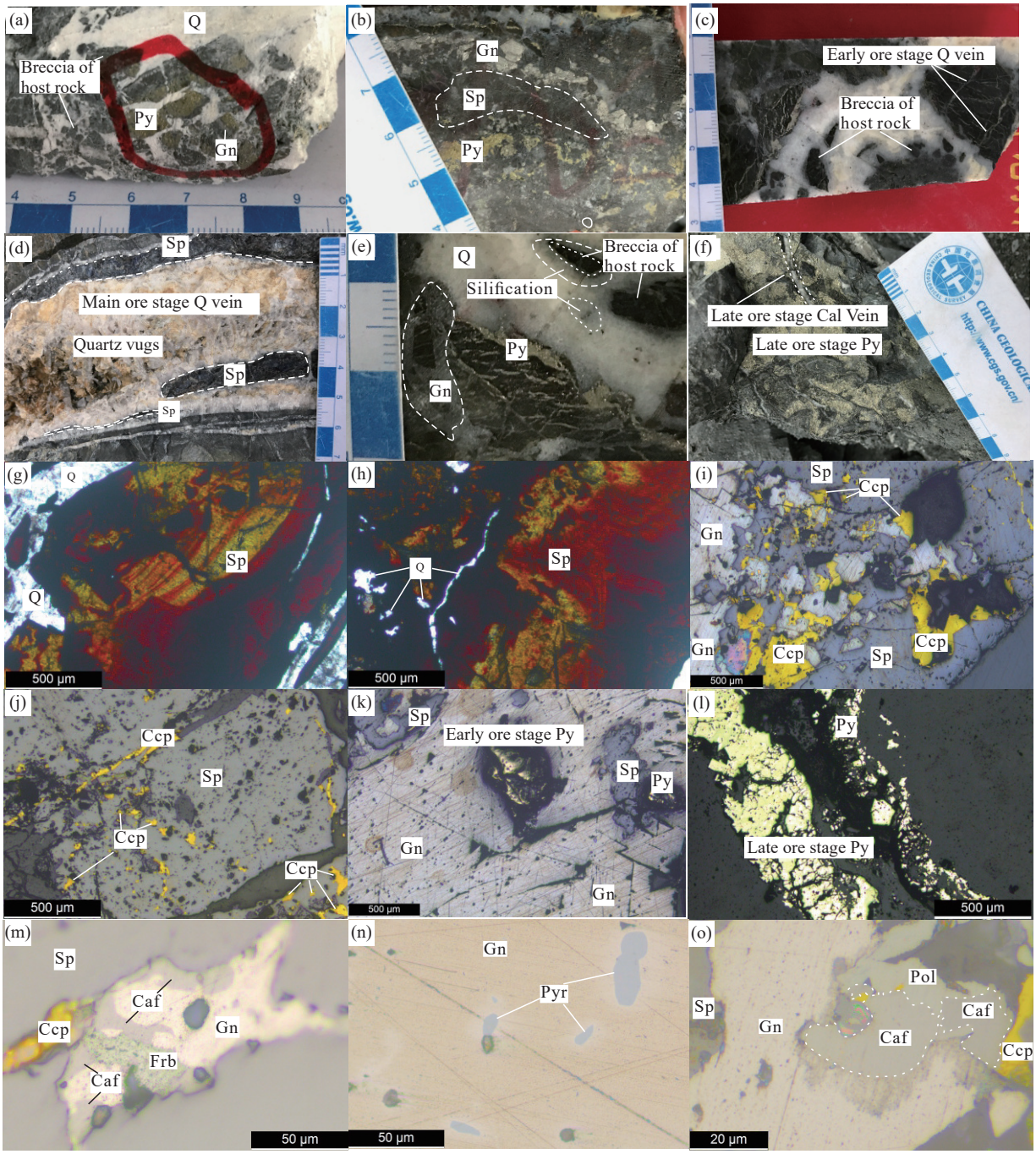

Fig. 5. Representative Pb-Zn-Ag ores and vein cutting relationships from the SJZ Ag-Pb-Zn deposit. a–hydrothermal breccia of host rock; b–c–hydrothermal breccia of host rock and early-ore-stage quartz vein in the breccia of host rock; d–quartz crystallized around breccia/fragments of hostrocks and with sulfides filling in the vug and interstitial to quartz, minor chalcopyrite grains distributed in sulfide veins; e–layers of comb-textured quartz and galena; f–late-ore stage fine-grained xenomorphic pyrite and late-ore-stage calcite vein; g–h–zoned texture of sphalerite; i–chalcopyrite and sphalerite replacing galena and pyrite, and chalcopyrite veins fill in the fracture of sphalerite; j–vein-like chalcopyrite distributed in the sphalerite fracture; k–galena replacing pyrite; l–late-ore stage pyrite; m–sphalerite replacing chalcopyrite and galena, and galena intergrown with polybasite and freibergite; n–pyrargyrite occurs as intergrowths with galena; o–canfieldite and polybasite gains grown in the fissure between sphalerite and galena grains. Photomicrographs g–h were taken under transmitted plane-polarized light; i–l were taken under reflected plane-polarized light. Ccp–chalcopyrite; Gn–galena; Py–pyrite; Sp–sphalerite; Caf–canfieldite; Frb–freibergite; Pyr–pyrargyrite; Pol–polybasite; Q–quartz; Cal–calcite.

in externally heated nickel reaction vessels. Hydrogen was measured by reacting the H_2O with zinc at 550°C. As the standard for reducing H and O, the results are based on the Standard Mean Ocean Water (SMOW) and their precision was within ±0.2‰ for $\delta^{18}O$ and ±2‰ for δD.

The calcite samples collected from ore-bearing quartz–calcite veins/veinlets were crushed to about 200 mesh powders for carbon and oxygen isotope analyses, which were conducted by the Beijing Geoanalysis Company, Beijing. Using a Micromass MultiPrep preparation device interfaced with a dual-inlet Micromass Isoprime stable-isotope-ratio mass spectrometer, it adopted the phosphoric acid reaction

method of Liu HB et al. (2013) but performed the reaction at 90°C. The carbon isotopic compositions are reported in delta notation ($\delta^{13}C$) relative to the international reference standard for carbon isotopes, i.e., VPDB and the oxygen isotopic compositions are reported in delta notation ($\delta^{18}O$) relative to the VPDB and VSMOW. The precision of the analyses was better than ±0.2‰.

4.2. He-Ar isotope analysis

Test analysis of the He-Ar isotope has been conducted by a MI- 1201IG inert gas mass spectrometer at the Institute of Mineral Resources, Chinese Academy of Geological Sciences (CAGS). Analytical methods are similar to Kendrick MA and Burnard P (2013). Approximately 200–1000 mg of 0.5–1.0 mm grains were loaded into vacuum crushers and atmospheric gases have been removed by baking on-line at less than 150°C for more than 24 hours. Gases were released from the grains into the all metal extraction system by sequential crushing in modified Nupro type valves. The released gases were exposed to a titanium sponge furnace at 800°C for 20 mins to remove the bulk of active gases (i.e., H_2O and CO_2), and then exposed to two SAES Zr-Al getters (one at room temperature, the other at 450°C) for 10 mins for further purification. Helium was separated from argon using an activated charcoal cold finger at liquid N_2 temperature (−196°C) for 40–60 mins to trap argon. Gas abundances were measured by peak-height comparison with known amounts of standard air from an air bottle. Procedural blanks were < 2×10^{-10} cm^3 STP ^4He and 2×10^{-10}–4×10^{-10} cm^3 STP ^{40}Ar and constituted<1% of analyzed samples. The blanks were too low to affect the calibration of the abundance measurements.

4.3. In-situ S and Pb isotope analysis

All *in-situ* isotope samples were collected from different mining levels (+350 m to +200 m). The authors performed mineralogical observations of 22 polished thin sections of sulfide ore and selected seven polished thin sections (massive and veinlet ores) representing three mineralization stages at the SJZ Ag-Pb-Zn deposit for *in-situ* sulfur isotope analysis and three polished thin sections (veinlets ores) for *in-situ* lead isotope analysis.

The authors performed *in-situ* sulfur isotopic analyses of sphalerite, galena, pyrite, and chalcopyrite using a Nu Plasma 1700 MC-ICP-MS (Nu instruments, UK), and used an NWR UP Femto (Electro Scientific Industries, Inc., USA) femtosecond laser ablation system as the ablation source for *in-situ* analysis at the State Key Laboratory of Continental Dynamics, Northwest University, Xian, China.

The NWR UP Femto femtosecond laser ablation system consists of a Quantronix Ti: Sapphire femtosecond laser amplifier Integra-HE and an ESI NWR Femto laser ablation system. The laser ultraviolet wavelength was 266 nm, which is the third harmonic of 800 nm, and its pulse duration was less than 130 fs. This instrument is equipped with a two-volume chamber with a large sample chamber (5000 cm^3) and a high-sensitivity sample cell (1.6 cm^3). The Nu 1700 MC-ICP-MS is equipped with 16 Faraday cups and three ion counters. The cup configurations for sulfur were an H5 cup for 34S, an Ax cup for 33S, and an L4 cup for 32S. Serious interference occurred from molecular ions, especially oxygen species, which were mixed with the sulfur peaks. The data acquisition type was static and the signal-analysis protocol included 30 cycles with an 8-s integration time per cycle. Two vials of pure water were used as the washer, with a total washing time of 140 s. Details regarding the fs-LA-MCICPMS *in-situ* S isotope analysis and instrument parameters are available in papers by Bao ZA et al. (2016a, 2016b) and Chen L et al. (2016).

The authors conducted *in-situ* lead isotope analyses of galena on 50 μm to 100 μm-thick polished sections, using a Nu Plasma™ multi-collector ICPMS with a femtosecond laser ablation system (NWR UPFemto, ESI, USA) (fLA-MC-ICPMS) at the State Key Laboratory of Continental Dynamics, Northwest University, Xian, China. The surfaces of the polished thin sections were cleaned using Milli-Q (18.2 MΩ cm) water before analysis. It then performed line-scan ablation, which consisted of background collection for 20 s followed by 50 s of laser ablation for signal collection. The laser ablation parameters are as follows: Spot size, 15 μm; 100% output energy, >600 μJ; 100% energy density, 6 J/cm^2; laser frequency, 5 Hz to 50 Hz; and ablation line rate, 3 μm/s, which ensures a strong enough Pb signal for the analysis of galena. The Tl (20×10^{-9}, NISTSRM 997, 205Tl/203Tl = 2.38890) and NIST SRM 610 glass served as internal and external standards, respectively. Repeated analyses of the NIST SRM 610 glass standard yielded highly reliable and reproducible results throughout the analytical process, with the means $^{206}Pb/^{204}Pb = 17.052 \pm 0.003$, $^{207}Pb/^{204}Pb = 15.515 \pm 0.003$, and $^{208}Pb/^{204}Pb = 36.980 \pm 0.007$ (1s, n = 183). Details regarding fs-LA-MCICPMS *in-situ* Pb isotope analysis and the instrument parameters are available in the works of Yuan HL et al. (2015) and Bao ZA et al. (2016).

4.4. Bulk Pb isotope analysis

The authors collected two diorite porphyrite and five Dashizhai Formation slate samples from underground mining tunnels and drill holes for bulk Pb isotope analysis. Fig. 4 shows the locations of these samples.

The fresh diorite porphyrite shows a gray-green color and a porphyritic structure (Fig. 4c). Phenocrysts (ca. 35 vol.%) in the diorite porphyry are plagioclase ca. 20 vol.% (1–2 mm) (Fig. 4c) and amphibole ca. 10 vol.% (1 mm) with minor biotite ca. 5 vol.% (0.5 mm). The matrix consists of plagioclase ca. 60 vol.% (0.1–0.2 mm), amphibole ca. 35 vol.% (0.05–0.10 mm) with minor biotite ca. 5 vol.% (ca. 0.05 mm), and disseminated pyrite, sphalerite, and galena mineralizations.

Pb isotopic composition measurements were performed on a Nu II MC-ICP-MS Instrument (Nu Instrument, Wrexham, UK) at the State Key Laboratory of Continental Dynamics,

Northwest University, Xi 'an, and the Beijing Geoanalysis Company. During the analyses, L4, L3, L2, L1, Ax, H1, and H2 Faraday cups were used to collect the ^{202}Hg, ^{203}Tl, ^{204}Hg+^{204}Pb, ^{205}Tl, ^{206}Pb, ^{207}Pb, and ^{208}Pb ion beams, respectively. The solution was self-aspirated at an uptake rate of 100 μL/mi through a standard PFA nebulizer and then desolvated by the AridusTM. The solution standards of the NIST NBS-981 adopted with NIST NBS-997 were measured along with the samples during the same MC-ICP-MS runs. The data were corrected for mass fractionation by normalizing them to ^{205}Tl/^{203}Tl=2.3889 using an exponential law. The Pb isotope analyses consist of two blocks with 20 cycles per block and an integration time of 10 s per cycle. The wash-out time (180 s) and time for transfer sample (120 s) resulted in an average instrument time of 12 mins per data. In this study, the measured NBS-981values agreed well with the recommended values of ^{208}Pb/^{206}Pb = 2.1674 ± 0.0005, ^{207}Pb/^{206}Pb = 0.91486 ± 0.00025, ^{206}Pb/^{204}Pb = 16.9397 ± 0.0111, ^{207}Pb/^{204}Pb = 15.4974 ± 0.0089, and ^{208}Pb/^{204}Pb = 36.7147 ± 0.0262, as recommended by Yuan HL et al. (2016). Finally, the Pb isotopic ratios were accurately determined after correction and were normalized to the SRM 981.

5. Analytical results

5.1. C, H, and O isotope analyses

Table 1 lists the hydrogen and oxygen isotope data, which are also shown in Fig. 6. The measured δ^{18}O values of five representative quartz samples and two calcite samples from different mineralization stages range from 6.3‰ to 16.2‰. The calculated $\delta^{18}O_{H2O}$ values from the early–ore to late–ore stages range from 7.7‰ to 9.1‰, from 7.5‰ to 7.9‰, and 1.8‰ to 3.8‰, respectively. The δD values of the FIs in the hydrothermal quartz samples ranged from −119‰ to −69‰, with an average of −98‰.

Table 2 and Fig. 7 show the C-O isotopic composition of calcite. The samples from ore-bearing calcite veins were measured to have δ^{13}C values ranging from −11.7‰ to −8.1‰ (mean = −9.9 ‰) (Fig. 7), which are within the typical range of mantle CO_2 (Clark I and Fritz P, 1997). The δ^{18}O values for the ore-calcite samples ranged from −3.5‰ to 3.2‰ (mean = 0.5333‰) (Table 2; Fig. 7).

5.2. He-Ar isotope

Noble gas abundance and isotopic data are listed in Table 3. The analytical results show that ^{40}Ar and ^{4}He concentrations range from 150×10^{-9} ccSTP/g to 470 ×10^{-9} ccSTP/g and 40×10^{-9} ccSTP/g to 90×10^{-9} ccSTP/g, respectively. Measured ^{40}Ar/^{36}Ar ratios range from 306.3 to 321.1. The ^{36}Ar/^{38}Ar ratios of fluid inclusions in all analyzed samples are relatively uniform and show a narrow range of 0.165–0.187 with an average of 0.179. The ^{3}He/^{4}He ratios of fluid inclusions hosted in sulfides are mainly from 0.33 to 0.78 Ra with an average of 0.54 Ra, where Ra represents the ^{3}He/^{4}He ratios of the atmosphere with a value of 1.4×10^{-6} (Mamyrin BA and Tolstikhin LN, 1984). The value of $^{4}He_{Mantle}$ is 5.4 % to 12.8 %, and the value of F^{4}He is a range of 160.5–763.0 (Fig. 8).

5.3. In-situ S and Pb isotopes

Table 4 lists the *in-situ* S isotopic compositions of the sulfide samples. The δ^{34}S values of the early-ore stage pyrite grains range from −2.3‰ to 0.2‰ (10 analyses) (Figs. 9a, 10a; Table 4), which are comparable to the main-ore stages of sphalerite (−2.5‰ to +0.5‰; 15 analyses), chalcopyrite (−1.5‰ to 0.1‰; 10 analyses), galena (−2.7‰ to −1.4‰; 11 analyses), and pyrite (−3.0‰ to −0.7‰; 10 analyses)(Figs. 9b, 10b). The δ^{34}S values of the post-ore pyrite grains range from −0.3‰ to 2.3‰ (seven analyses; Figs. 9c, 10c; Table 4). The δ^{34}S values of the syenogranite sulfide grains range from

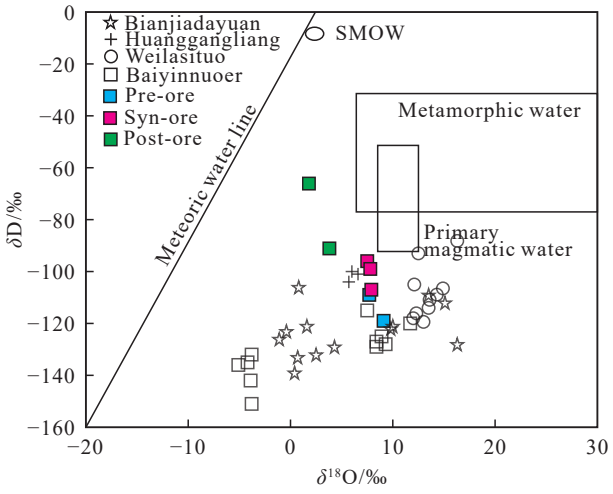

Fig. 6. δD *vs.* δ^{18}O diagram of the ore-forming fluids in the SJZ Ag-Pb-Zn deposit. Isotopic compositions of magmatic and metamorphic waters after Taylor HP (1974), and meteoric water line after Craig H (1961). Coeval deposit D-O isotope compositions after Mei W et al., 2015; Ouyang GH et al., 2014, 2015.

Table 1. H and O isotope compositions of the ore fluids in the SJZ Ag-Pb-Zn deposit.

Sample No.	Stage	Mineral	δD/‰	$\delta^{18}O_{SMOW}$/‰	$\delta^{18}O_{H2O}$/‰	Th/°C
I-4-1	Early-ore	Quartz	−109	13.5	7.7	310
I-4-2			−119	15.7	9.1	307
ZK1807-4	Main-ore		−99	16.2	7.8	273.4
ZK1807-5			−107	6.3	7.9	263.8
ZK1807-6			−96	15.9	7.5	259
Zk1601-13	Late-ore	Calcite	−66.1	12.5	1.8	217.6
ZK1601-12			−91.1	12	3.8	217.4

Table 2. C and O isotope compositions of calcites in the SJZ Ag-Pb-Zn deposit (‰).

Sample No.	$\delta C_{V\text{-}PDB}$	$\delta O_{V\text{-}PDB}$	$\delta O_{V\text{-}SMOW}$
ZK1515-2	−11.5	−28.3	1.8
ZK1601-1	−10	−30.1	−0.1
SJZS1712-8	−9.2	−28.4	1.6
SJZS1712-4	−11.8	−21	9.2
SJZS1712-5	−8.1	−33.3	−3.5
SJZS1713-1	−11.7	−26.8	3.2
SJZS1778-5	−8.9	−29.7	0.2

−1.1‰ to 0.5‰ (eight analyses; Figs. 9d, 10d; Table 4).

Table 5 lists the *in-situ* lead isotopic compositions of galena. The $^{206}Pb/^{204}Pb$, $^{208}Pb/^{204}Pb$, and $^{207}Pb/^{204}Pb$ ratios of the galena grains in the ZK1601-2 sample range from 18.291 to 18.295 (average of 18.292), 38.148 to 38.162 (average of 38.153), and 15.545 to 15.550 (average of 15.547), respectively (Figs. 9a, 11; Table 5). The $^{206}Pb/^{204}Pb$, $^{208}Pb/^{204}Pb$, and $^{207}Pb/^{204}Pb$ ratios of the galena grains in the ZK1601-14 sample range from 18.291 to 18.299 (average of 18.294), 38.143 to 38.167 (average of 38.159), and 15.544 to 15.553 (average of 15.549), respectively (Figs. 9b, 11; Table 5). The $^{206}Pb/^{204}Pb$, $^{208}Pb/^{204}Pb$, and $^{207}Pb/^{204}Pb$ ratios of the galena grains in the ZK1601-3 sample range from 18.288 to 18.296 (average of 18.290), 38.143 to 38.167 (average of 38.157), and 15.544 to 15.553 (average of 15.545), respectively (Figs. 9c, 11; Table5). The $^{206}Pb/^{204}Pb$, $^{208}Pb/^{204}Pb$, and $^{207}Pb/^{204}Pb$ ratios of the galena grains in the ZK1237-2 sample range from 18.301 to 18.309 (average of 18.305), 38.153 to 38.171 (average of 38.162), and 15.544 to 15.550 (average of 15.547), respectively (Figs. 9d, 11; Table 5).

5.4. Bulk Pb isotope analysis

Table 5 lists the bulk Pb isotope compositions of slate, syenogranite, and diorite porphyrite. The $^{206}Pb/^{204}Pb$, $^{208}Pb/^{204}Pb$, and $^{207}Pb/^{204}Pb$ ratios of the syenogranite samples range from 18.844 to 19.009 (average of 18.834), 38.571 to 38.785 (average of 38.641), and 15.573 to 15.588 (average of 15.578), respectively (Fig. 11; Table 5). The $^{206}Pb/^{204}Pb$, $^{208}Pb/^{204}Pb$, and $^{207}Pb/^{204}Pb$ ratios of the diorite

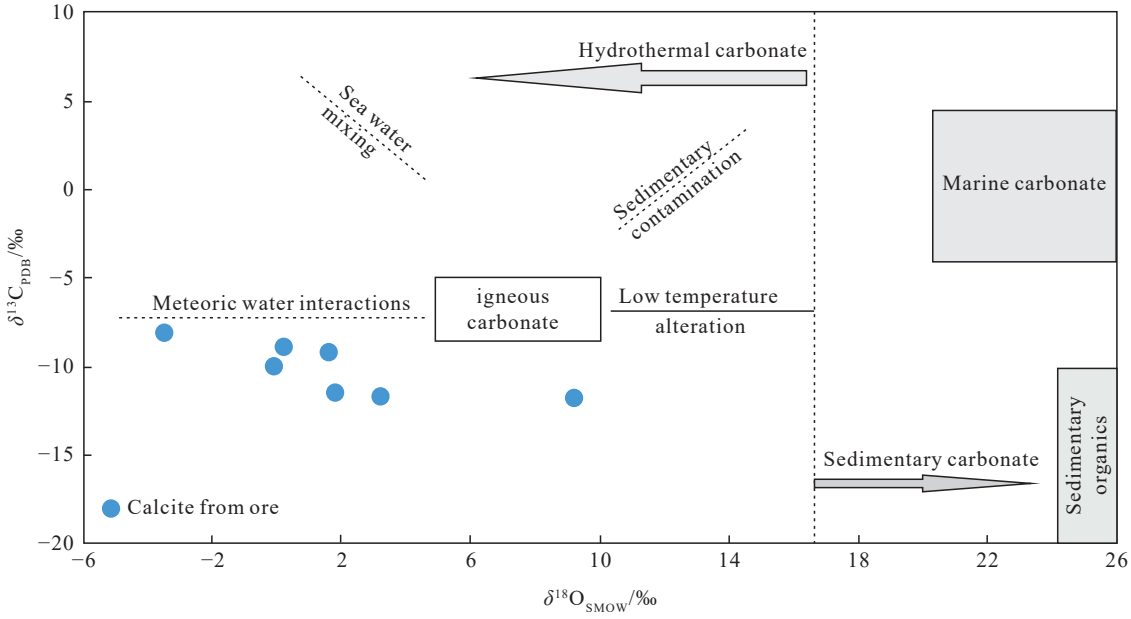

Fig. 7. $\delta^{13}C_{PDB}$ *vs.* $\delta^{18}O_{SMOW}$ diagram of the calcite in the SJZ Ag-Pb-Zn deposit (after Liu YF et al., 2017).

Table 3. He and Ar isotope compositions of sphalerite in the SJZ Ag-Pb-Zn deposit.

Sample No.	$^4He(10^{-7}$ ccSTP/g)	$^3He/^4He$ (Ra)	^{40}Ar (10^{-7}ccSTp/g)	$^{40}Ar/^{36}Ar$	$^{38}Ar/^{36}Ar$	$^*Ar$	$^*Ar/^4He$	F^4He	He_{mantle}/%
ZK1807-1	0.8	0.33±0.05	2.6	318.6±3.5	0.180±0.003	0.19	0.57	582.5	5.4
ZK1807-2	0.9	0.38±0.09	2.4	320.9±4.8	0.165±0.006	0.19	0.50	721.9	6.2
ZK1807-3	0.9	0.51±0.03	4.7	306.3±3.0	0.186±0.001	0.17	0.33	367.0	8.3
ZK1807-5	0.6	0.78±0.10	1.5	321.1±3.6	0.177±0.003	0.12	0.16	763.0	12.8
ZK1808-2	0.4	0.72±0.06	4.6	306.4±3.0	0.187±0.001	0.16	0.23	160.5	11.9

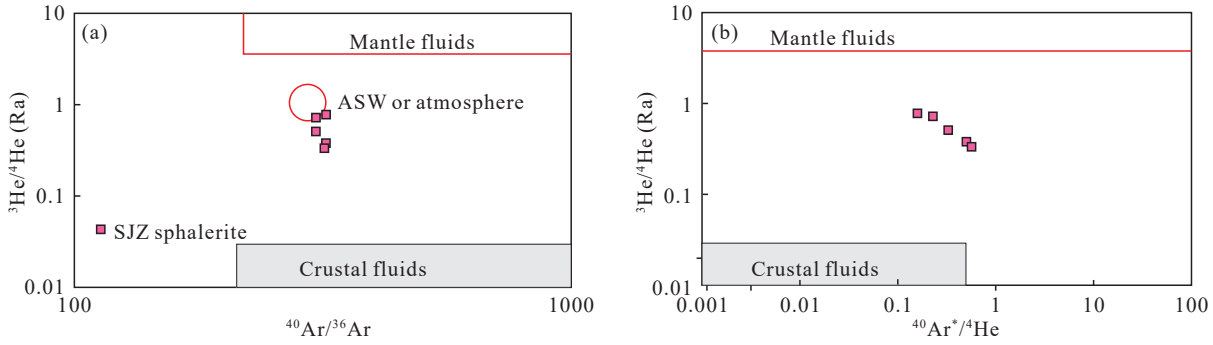

Fig. 8. $^3He/^4He$ *vs.* $^{40}Ar/^{36}Ar$ diagram (a), and $^3He/^4He$ *vs.* $^{40}Ar^*/^4He$ (b) of fluid inclusions in sphalerite from the SJZ Ag-Pb-Zn deposit.

Table 4. Sulfur isotopic compositions of sulfides in the SJZ Ag-Pb-Zn deposit.

Stage	No.	Object	$\delta^{34}S$/‰	Stage	No.	Object	$\delta^{34}S$/‰
Early-ore stage	SJZS179-9.2	Pyrite	−0.5	Syn-ore stage	ZK1601-14.1.1	Galena	−2.3
	SJZS179-9.3	Pyrite	0.4		ZK1601-14.1.4	Galena	−2.3
	SJZS179-9.4	Pyrite	−0.9		ZK1601-14.4.1	Galena	−1.9
	SJZS179-9.5	Pyrite	−2.1		ZK1601-14.5.1	Galena	−2.3
	ZK1601-2.1	Pyrite	−0.1		ZK1601-14.5.2	Galena	−2.0
	ZK1601-2.4	Pyrite	−1.1		ZK1601-14.9.2	Galena	−2.9
	ZK1601-2.5	Pyrite	−2.3		ZK1601-14.9.3	Galena	−2.8
	ZK1601-3.5	Pyrite	−1.3		ZK1601-3.1	Galena	−1.4
	ZK1601-3.6	Pyrite	−1.1		ZK1601-2.1	Galena	−2.7
	ZK1601-3.13	Pyrite	−1.5		ZK1601-20.1	Pyrite	−0.7
	ZK1601-3.14	Pyrite	−0.9		ZK1601-20.2	Pyrite	−2.5
	ZK1601-3.15	Pyrite	−1.2		ZK1601-20.3	Pyrite	−2.7
	ZK1601-3.16	Pyrite	−1.1		ZK1601-20.4	Pyrite	−2.8
Syn-ore stage	ZK1601-14.8.2	Chalcopyrit	−1.1		ZK1601-20.7	Pyrite	−3.0
	ZK1601-14.5.4	Chalcopyrit	−0.9		ZK1601-20.8	Pyrite	−2.3
	ZK1601-14.4.2	Chalcopyrit	−0.9		ZK1601-20.10	Pyrite	−3.0
	ZK1601-14.9.4	Chalcopyrit	−1.5	Post-ore Stage	ZK1601-13.1	Pyrite	2.1
	ZK1601-3.17	Chalcopyrit	−0.8		ZK1601-13.3	Pyrite	2.1
	ZK1601-3.18	Chalcopyrit	−1.0		ZK1601-13.4	Pyrite	2.3
	ZK1601-3.20	Chalcopyrit	−1.5		ZK1601-13.5	Pyrite	2.0
	ZK1601-14.5.3	Sphalerite	−0.4		ZK1601-13.6	Pyrite	−0.1
	ZK1601-14.9.1	Sphalerite	−0.3		ZK1601-13.7	Pyrite	0.3
	ZK1601-3.2	Sphalerite	−0.9		ZK1601-13.8	Pyrite	−0.3
	ZK1601-3.3	Sphalerite	0.1		ZK1601-13.9	Pyrite	0.5
	ZK1601-3.8	Sphalerite	0.5		ZK1601-13.10	Pyrite	1.2
	ZK1601-3.9	Sphalerite	−1.0	syenogranite	ZK1237-2.1	Sphalerite	0.5
	ZK1601-3.10	Sphalerite	−0.8		ZK1237-2.2	Sphalerite	0.1
	ZK1601-3.11	Sphalerite	−0.2		ZK1237-2.3	Sphalerite	−0.9
	ZK1601-2.3	Sphalerite	−0.0		ZK1237-2.4	Sphalerite	−1.1
	ZK1601-21.1	Sphalerite	−1.5		ZK1237-2.5	Galena	−0.4
	ZK1601-21.2	Sphalerite	−2.5		ZK1237-2.6	Galena	−0.3
	ZK1601-21.3	Sphalerite	−1.7		ZK1237-2.7	Galena	−0.0
	ZK1601-21.4	Sphalerite	−1.0		ZK1237-2.8	Galena	−0.6

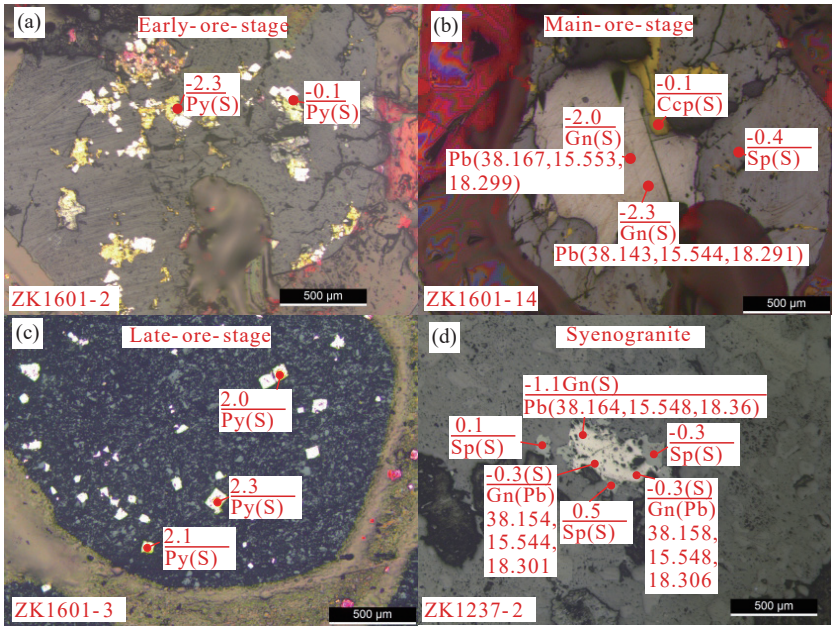

Fig. 9. Photomicrographs in reflected light showing the location of *in-situ* S and Pb isotope values of pyrite, galena, and sphalerite. a–pre-ores stage pyrite; b–syn-ore stage sphalerite, chalcopyrite, galena, and pyrite; c–post-ore pyrite; d–The syenogranite. Py–pyrite; Sp–sphalerite; Gn–galena; Ccp–chalcopyrite.

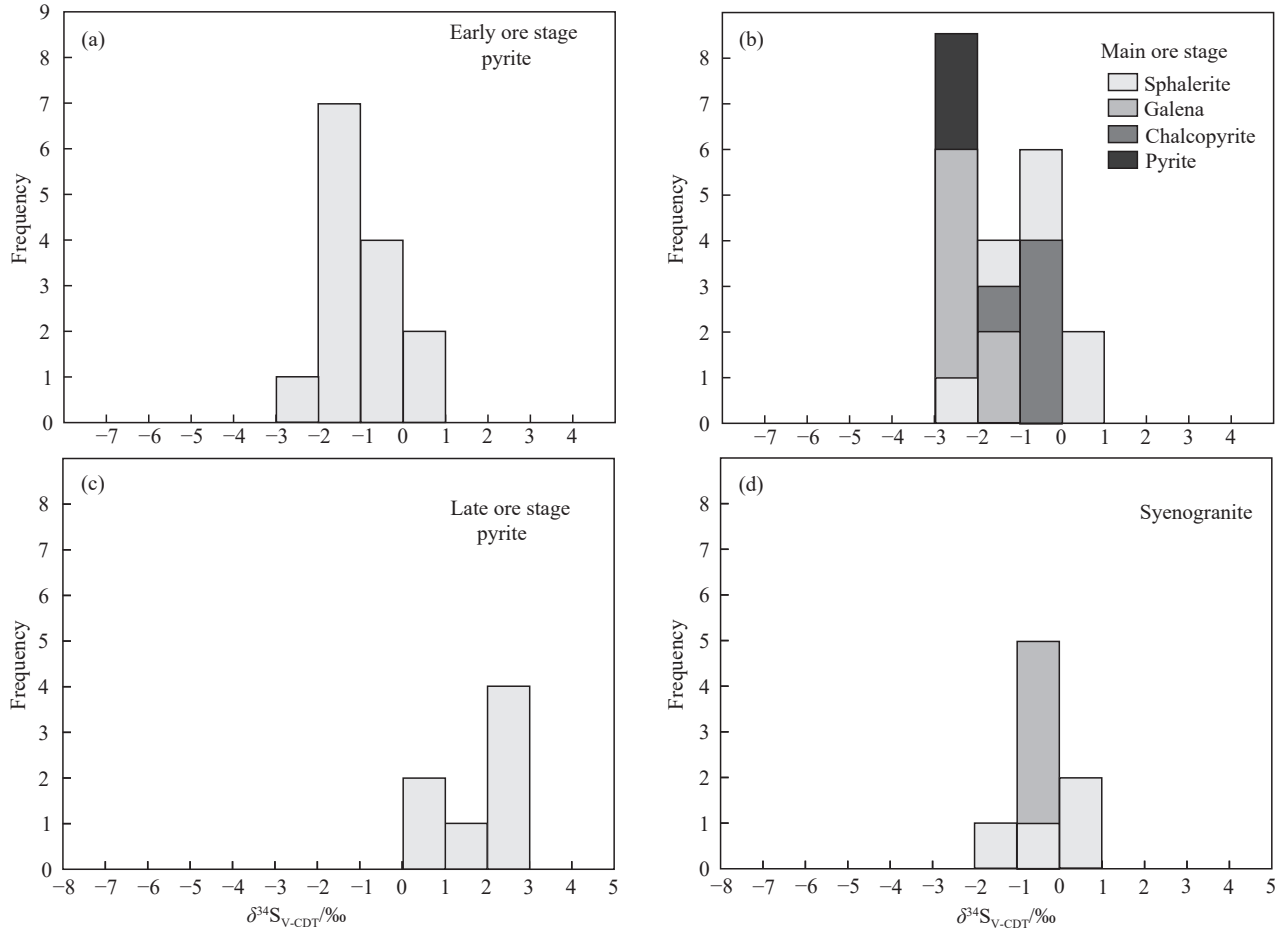

Fig. 10. The $\delta^{34}S$ of representative sulfide in the different ore stages and syenogranite.

porphyry samples range from 18.285 to 18.323 (average of 18.299), 38.149 to 38.224 (average of 38.179), and 15.541 to 15.55 (average of 15.545), respectively. The $^{206}Pb/^{204}Pb$, $^{208}Pb/^{204}Pb$, and $^{207}Pb/^{204}Pb$ ratios of the slate samples range from 18.279 to 18.288 (average of 18.284), 38.112 to 38.120 (average of 38.116), and 15.308 to 15.535 (average of 15.533), respectively (Fig. 11; Table 5).

6. Discussion

6.1. Sources of ore-forming fluids

Previous studies suggest that the combined application of multiple isotopic analyses is an effective way to trace the sources of ore-forming fluids (Zhai DG et al., 2018a, 2020).

The SJZ ore-bearing quartz and calcite veins have relatively high $\delta^{18}O_{H2O}$ values (7.5‰ to 9.1‰ and 1.8‰ to 3.8‰, respectively), which is consistent with those reported in other magmatic-hydrothermal deposits in the SGHR (Ouyang HG et al., 2014, Zhai DG et al., 2018a), suggesting a magmatic signature (Cooke DR et al., 2011) (Fig. 6). In contrast, they have low δD_{H2O} values (−119‰ to −66.1‰). Zhai DG et al. (2018a) and Zhang HY et al. (2019) pointed out that low δD_{H2O} values could be caused by fluid mixing between meteoric fluid and ore fluid. Combing with the $\delta^{18}O_{H2O}$ values of these samples showing a remarkable decline from the early to late stage (Fig. 6), the authors infer that the SJZ ore-forming fluid was originated from magmatic water and diluted by meteoric water in the late-ore stage.

The $\delta^{13}C$ values of the SJZ post-ore stage calcite range from −11.7‰ to −8.1‰, which indicates a dominant magmatic origin for the carbon (−9‰ to −3‰, Taylor HP et al., 1967). Besides, such variation of the $\delta^{18}O$ values (−3.5‰ to 3.2‰), suggests meteoric water mixing (Fig. 7). These C-O isotope features indicating that the SJZ late ore stage calcite-veins precipitation from magmatic water with the mixing of the meteoric water.

The $^{3}He/^{4}He$ ratios of fluid inclusions extracted from sphalerite show higher values (0.33–0.78 Ra) than the value of crust-derived He (0.01–0.05 Ra, Stuart FM et al., 1994). However, the obtained $^{3}He/^{4}He$ ratios of sphalerite in the deposit are significantly lower than the value of mantle-derived He (6–7 Ra). In the $^{3}He/^{4}He$ *vs.* $^{40}Ar/^{36}Ar$ (Fig. 8a) and $^{40}Ar^{*}/^{4}He$ (Fig. 8b) plots, the noble gas isotopic data plotted between the mantle and crust field, suggesting a hybrid-He source. Besides, crust-mantle dual model: He_{mantle} (%) = (R-R_C) / (R_M-R_C) × 100%, where R_M = 8, R_C = 0.01 and R represent the $^{3}He/^{4}He$ ratios of the fluids in the mantle, crust, and the sample (Kendrick MA et al., 2001; Tolstikhin IN, 1978), the calculated results of the percentage of the mantle He from the SJZ Ag-Pb-Zn deposit are in the range of 5.4%–12.8%, with an average of 8.9%. These values indicate that the ore-forming fluids are dominated by crustal fluids

with only a minor contribution from the mantle. The measured $^{40}Ar/^{36}Ar$ values of fluid inclusions hosted in the SJZ sphalerite range from 306.3 to 320.9 (average 314.7), which are close to the value of the air-saturated water (295.5), but much lower than those of mantle and crust-derived Ar (Stuart FM et al. 1994). In the $^{3}He/^{4}He$ *vs.* $^{40}Ar/^{36}Ar$ diagram (Fig. 8a), all data points plot in the field between the ASW and crustal end members. Therefore, the SJZ ore-forming fluids might be a mixture of crustal fluid and meteoric water.

In summary, the C-D-O-He-Ar isotope compositions indicate that the SJZ ore-forming fluids originated from a mixture source between crustal-derived magmatic-

Table 5. Pb isotopic compositions of sulfides in the SJZ Ag-Pb-Zn deposit.

No.	Object	$^{206}Pb/^{204}Pb$	1s	$^{207}Pb/^{204}Pb$	1s	$^{208}Pb/^{204}Pb$	1s	$^{208}Pb/^{206}Pb$	1s	$^{207}Pb/^{206}Pb$	1s	μ
ZK1601-14.1.1	Galena in the mineral-izaed veins	18.295	0.004	15.550	0.004	38.167	0.011	2.0860	0.0002	0.84992	0.00004	9.380
ZK1601-14.1.4		18.295	0.004	15.550	0.004	38.164	0.012	2.0861	0.0002	0.84991	0.00004	9.380
ZK1601-14.4.1		18.294	0.003	15.549	0.003	38.158	0.009	2.0859	0.0001	0.84991	0.00003	9.380
ZK1601-14.5.1		18.291	0.003	15.544	0.003	38.143	0.008	2.0857	0.0001	0.84984	0.00003	9.370
ZK1601-14.5.2		18.299	0.003	15.553	0.003	38.167	0.009	2.0861	0.0002	0.84995	0.00004	9.380
ZK1601-14.8.2		18.292	0.003	15.547	0.003	38.154	0.009	2.0861	0.0001	0.84996	0.00004	9.370
ZK1601-2.1		18.295	0.004	15.550	0.004	38.162	0.012	2.0860	0.0002	0.84994	0.00005	9.380
ZK1601-2.2		18.291	0.004	15.547	0.004	38.150	0.012	2.0861	0.0002	0.84995	0.00005	9.370
ZK1601-2.3		18.292	0.004	15.547	0.004	38.153	0.010	2.0861	0.0002	0.84999	0.00004	9.370
ZK1601-2.5		18.291	0.004	15.545	0.005	38.148	0.013	2.0857	0.0002	0.84986	0.00005	9.370
ZK1601-3.1		18.288	0.004	15.544	0.004	38.146	0.012	2.0859	0.0002	0.84995	0.00005	9.370
ZK1601-3.2		18.292	0.005	15.547	0.005	38.149	0.013	2.0858	0.0002	0.84986	0.00005	9.370
ZK1601-3.3		18.296	0.004	15.552	0.004	38.160	0.013	2.0861	0.0002	0.84997	0.00005	9.380
ZK1601-3.4		18.287	0.004	15.542	0.004	38.137	0.011	2.0858	0.0002	0.84990	0.00004	9.360
ZK1601-3.5		18.286	0.004	15.541	0.004	38.149	0.020	2.0858	0.0003	0.84991	0.00005	9.360
ZK1601-3.6		18.291	0.004	15.547	0.004	38.153	0.011	2.0861	0.0002	0.84994	0.00004	9.370
ZK1237-2.5	Galena in the syengra-nite	18.301	0.004	15.544	0.004	38.154	0.011	2.0849	0.0002	0.84932	0.00004	9.37
ZK1237-2.6		18.306	0.003	15.548	0.004	38.164	0.010	2.0850	0.0002	0.84931	0.00004	9.37
ZK1237-2.7		18.307	0.003	15.550	0.004	38.171	0.010	2.0851	0.0002	0.84938	0.00004	9.38
ZK1237-2.8		18.306	0.003	15.548	0.003	38.158	0.008	2.0847	0.0001	0.84930	0.00003	9.37
ZK1237-2.9		18.306	0.003	15.548	0.003	38.162	0.009	2.0849	0.0001	0.84933	0.00003	9.37
ZK1237-2.10		18.301	0.003	15.544	0.003	38.153	0.009	2.0848	0.0001	0.84933	0.00004	9.37
ZK1237-2.11		18.309	0.003	15.550	0.003	38.168	0.009	2.0850	0.0002	0.84938	0.00004	9.38
SJZS1021-6	Diorite-Porphyrite	18.290	0.0006	15.542	0.0004	38.165	0.0014	2.08669	0.00003	0.849766	0.000013	9.360
SJZS1021-7		18.285	0.00076	15.541	0.00063	38.149	0.00210	2.08634	0.00005	0.84995	0.00002	9.360
ZK1601-5	Black slate	18.288	0.0006	15.535	0.0005	38.120	0.0011	2.084417005	0.00003	0.849465883	0.000012	9.350
ZK1601-6		18.283	0.0007	15.531	0.0006	38.116	0.0016	2.084821416	0.00004	0.849484213	0.000015	9.340
ZK1601-7		18.286	0.0009	15.534	0.0008	38.116	0.0020	2.084433787	0.00003	0.849483165	0.000014	9.350
ZK1601-8		18.279	0.0006	15.531	0.0006	38.112	0.0015	2.0849782	0.00005	0.849640362	0.000011	9.340
ZK1601-9		18.282	0.0008	15.532	0.0007	38.115	0.0018	2.084802332	0.00002	0.849566598	0.000013	9.340

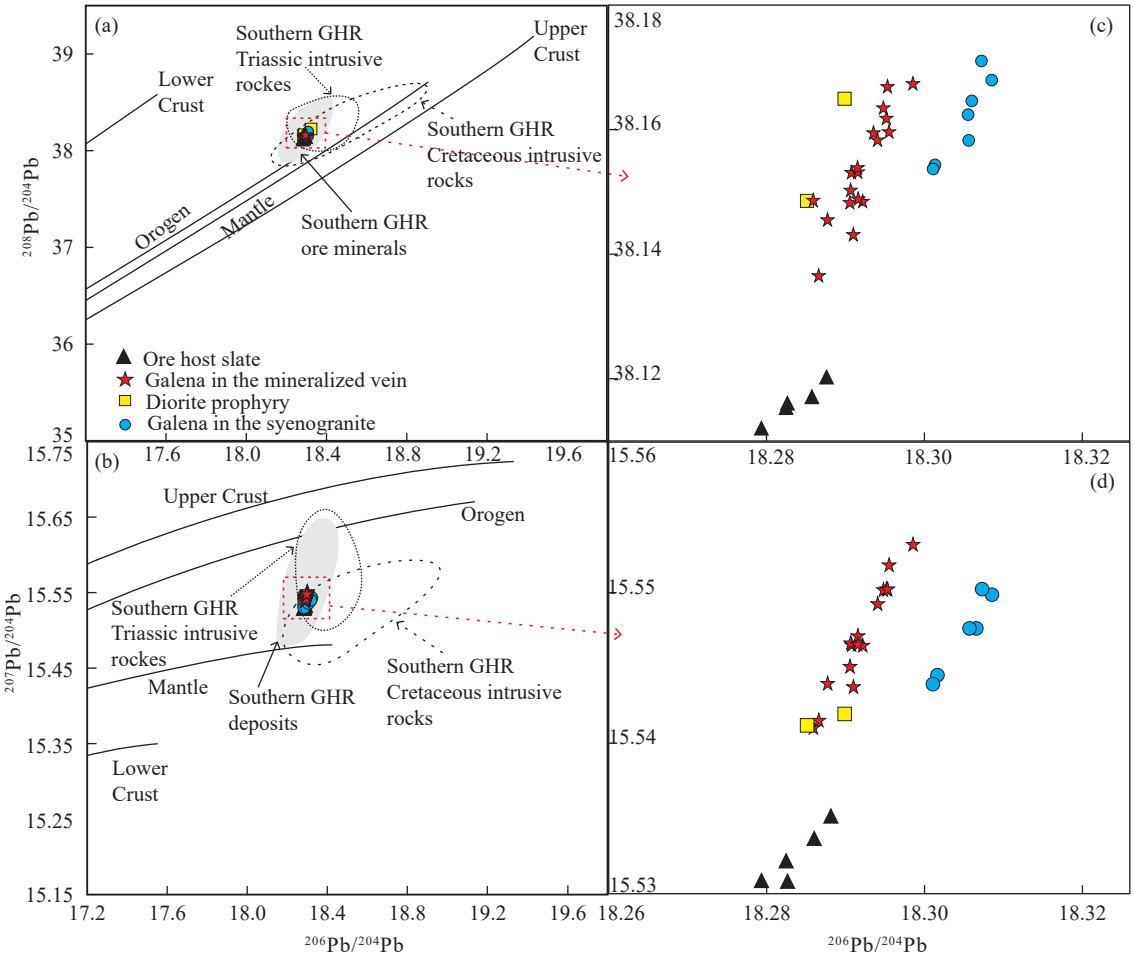

Fig. 11. a–*in-situ* $^{208}Pb/^{204}Pb$ *vs.* $^{206}Pb/^{204}Pb$ diagram; b–*in-situ* $^{207}Pb/^{204}Pb$ *vs.* $^{206}Pb/^{204}Pb$ diagram; c–*in-situ* $^{208}Pb/^{204}Pb$ *vs.* $^{206}Pb/^{204}Pb$ diagram that presents the comparison between *in-situ* and bulk Pb isotope data; d–*in-situ* $^{207}Pb/^{204}Pb$ *vs.* $^{206}Pb/^{204}Pb$ diagram that presents the Pb evolution curves of galena and diorite porphyry. The shadow area represents the Pb isotope component from the Haobugao deposit, Baiyinnuoer deposit, Huangganglang deposit, and Weilasituo deposit; the date from Jiang SH et al., 2010, 2011a, 2011b; Ouyang HG et al., 2014; Zhai DG et al., 2014; Liu LJ et al., 2018; the Triassic intrusive rocks data from Jiang SH et al., 2017; the Cretaceous intrusive rocks data from Jiang SH et al., 2017; Mei W et al., 2015; Ouyang HG et al., 2014; Zhai DG et al., 2014; the Upper Crust, Orogen, Mantle, Lower Crust Pb evolution lines from Zartman RE and Doe BR, 1981.

hydrothermal fluid and meteoric water. As mentioned above, disseminated sulfides have been observed in the syenogranite. Therefore, The authors infer that the SJZ ore-forming fluids originated from the syenogranite magmatic system.

6.2. Sources of sulfur and metal

Ohmoto H and Rye R (1979) and Rollinson H (1993) pointed out that the sulfur isotope is an efficient way to decipher the source of ore-forming materials. The $\delta^{34}S$ values of sulfide samples (galena, sphalerite, and pyrite) in the SJZ Ag-Pb-Zn deposit, with a limited range from −3.0‰ to +2.3‰, mostly between −3.0‰ and 0‰. These sulfide samples with uniform $\delta^{34}S$ values are consistent with the magmatic sulfur (Seal RR, 2006), which indicates a relatively constant physicochemical condition of the ore-forming fluids during ore precipitation. *In-situ* S isotope analysis shows that most of the pyrite, chalcopyrite, and sphalerite grains are enriched in $\delta^{34}S$ compared to galena in the main-ore-stage Ag-Pb-Zn veins (Table 4; Fig. 10), which indicates that sulfides were in equilibrium with ore-forming fluids. A few samples have more negative or positive values, most likely resulting from local variations of temperature, redox conditions (f_{O2}), and pH (Ohmoto H, 1972). Collectively, sulfides from the Baiyinnuoer, Haobugao, Bairendaba, Weilasituo, Huangganglang, and Bianjiadayuan deposits in the SGHR have $\delta^{34}S$ values mostly in the range of −4‰ to 5‰ (Jiang SH et al., 2010, 2011a, b, 2017; Ouyang HG et al., 2014,2015), which is consistent with other porphyries-, skarn- and hydrothermal- type deposits in the world (Meinert LD et al., 2005; Cooke DR et al., 2011). Therefore, the $\delta^{34}S$ enrichment in the SJZ Ag-Pb-Zn deposit is interpreted to have a magmatic sulfur origin (Ohmoto H, 1972; Seal RR, 2006).

In the $^{208}Pb/^{204}Pb$ *vs.* $^{206}Pb/^{204}Pb$ diagram, the majority of Pb isotope values plot in the field between the lower crust and orogenic belt evolution line, and are closer to the orogenic belt evolution line (Fig. 11a); Pb isotope values fall between the mantle and orogenic belt evolution line on the $^{207}Pb/^{204}Pb$ *vs.* $^{206}Pb/^{204}Pb$ diagrams. These features suggest the Pb was initially derived from the mantle and crustal mixture, with more affinity to crustal material. This view has been further proved by the μ values of the SJZ sulfides, the μ values range

from 9.36 to 9.38, with an average of 9.37, which are lower than upper crustal values (9.58) but higher than mantle values (8.92; Doe BR and Zartman RE, 1979), these features further demonstrates that the Pb of the SJZ Ag-Pb-Zn deposits was originated from a mixture Pb source. Notably, the Pb isotopic compositions of galena from ore-veins are broadly comparable to values of the disseminated galena from fine-grained syenogranite (Fig. 11). Moreover, the galena Pb isotopic data points of the sulfides present a linear correlation with the host slate (Fig. 11). The authors suggest that the fine-grained syenogranite magma and the Dashizhai Formation slate contributed most of the lead and ore-forming metals (Figs. 11a, b; Andrew A et al., 1984; Chiaradia M et al., 2006).

In summary, the Pb-S isotopic compositions of the SJZ sulfide are indicating that the SJZ ore-forming S and Pb generated from the crust-derived magma, which is consistent with most of the coeval ore deposits and intrusive rocks in the southern GHR (Ouyang HG et al., 2015, Zhai DG et al., 2019a). It is noteworthy that little proportion of metals from mantle-material has been observed (Fig 8, 11).

6.3. Causative intrusion

As mentioned above, three types of intrusive rocks have been exposed in the SJZ Ag-Pb-Zn deposit, that are diorite porphyrite, monzogranite, and syenogranite. The Ag-Pb-Zn mineralized veins crosscut the diorite porphyrite, and the diagenetic age of the diorite porphyrite (240.7 Ma) is significantly older than the Metallogenic age (135 Ma; Zhai DG et al., 2020). Besides, the monzogranite is a coarse-grained texture and is free of sulfides, and the zircon U-Pb age of monzogranite (142 Ma) is slightly older than the metallogenic age (Dai M et al., 2022). Previous studies pointed out that mineralization is usually a catastrophic event in the lithosphere, and the coarse-grained texture suggests magma underwent sufficient crystallization and homogenization, which is disadvantageous to the ore-forming elements enriching (Dai M et al., 2019; Luo ZH et al., 2010). According to the field investigation, petrographic observation, and the stable isotopic composition characteristics of the syenogranite, the authors infer that the mineralization of the SJZ Ag-Pb-Zn deposit has a close relationship with the syenogranite magmatic system. Therefore, the authors suggest that the syenogranite is the ore-forming intrusive rock in the SJZ Ag-Pb-Zn deposit.

First, the zircon U-Pb isotopic age of the monzogranite is 142 Ma (Dai M et al., 2022), which is slightly older than the syenogranite (140 Ma; Dai M et al., 2022), suggesting the syenogranite is not chilled margin part of the monzogranite. Moreover, the diagenetic age of the syenogranite is 135–140 Ma (Dai M et al., 2022, Zhai DG et al., 2020), which is consistent with the molybdenite and pyrite Re-Os isotopic model ages (135 Ma; Zhai DG et al., 2020). Second, the disseminated galena, sphalerite, and molybdenite have been observed in syenogranite (Fig. 4), and there is a cotectic texture between the sulfides and the quartz/feldspar in syenogranite, which suggesting they crystallized at the same time. Third, the disseminated sulfides in the syenogranite have comparable S-Pb isotopic composition with sulfides in the mineralized veins (Fig. 10, 11). Fourth, the have low $Mg^{\#}$, near zero whole-rock Nd isotopic compositions, positive zircon Hf isotopic compositions and juvenile TDM_2 ages (761–1091 Ma and 589–994 Ma), which suggest the primary magma of the syenogranite was derived from partial melting of the juvenile lower-crustal basaltic rocks (Dai M et al., 2022).

6.4. Evidence of crystal accumulation and high-silicic melt extraction

The syenogranite is charactered by higher SiO_2 (> 75%) and K_2O contents and lower MgO, TiO_2, and P_2O_5 concentrations than the monzogranite (Fig. 12; Table. 6), implying the syenogranite is the most evolved magmatic rocks. Although, the syenogranite and monzogranite have a gradually contact relationship and the same Sr-Nd-Hf isotopic compositions, they have different solidification processes.

The syenogranite and monzogranite show tight linear trends on the Harker diagram (Fig. 12). The monzogranite samples show relatively weak Eu negative anomaly (Eu= 0.29–0.41) and have relatively high CaO, TFe_2O_3, Mg, Al_2O_3, Ba and Sr contents and low K_2O and Rb concentrations (Figs. 12, 13), which could be interpreted by the deeper magma reservoir that had accumulated plagioclase, biotite, and Ti-Fe oxides. The incorporation of around 38% plagioclase and/or biotite is sufficient to raise the Sr content of the rock from about 140×10^{-6}–300×10^{-6} and the Eu content of the rock from 0.4×10^{-6} to 0.8×10^{-6} (Fig. 14) (see modeling discussion below). Abundant petrographic evidence demonstrates that the SJZ monzogranite has solidified largely through the accumulation of crystals in the magma reservoir (Fig. 14). Such as the aggregates of coarse-grained euhedral plagioclase crystals and aggregates of biotite crystals have been observed in the monzogranite, which is consistent with the physical accumulation of crystals (Vernon RH and Collins WJ, 2011). In addition, a framework of touching euhedral minerals dominated by plagioclase and alkali feldspar along with minor biotite and hornblende is interpreted by the cumulation of the earlier-formed euhedral minerals (Schaen AJ et al., 2018). The cores of plagioclase crystals have variable zonation histories (Fig. 4h), which suggests that they crystallized in different environments and accumulated together later before the crystallization of their rims (Beane R and Wiebe RA, 2012). Thus, according to these petrographic observations and the geochemical characteristics of the whole rocks, the monzogranite is interpreted to represent the cumulate residue of a crystal mush (or magma reservoir).

The fine-grained syenogranite has higher SiO_2, K_2O contents, and differentiation index (DI>92), lower Al_2O_3 and other major elements than the coarse-grained monzogranite

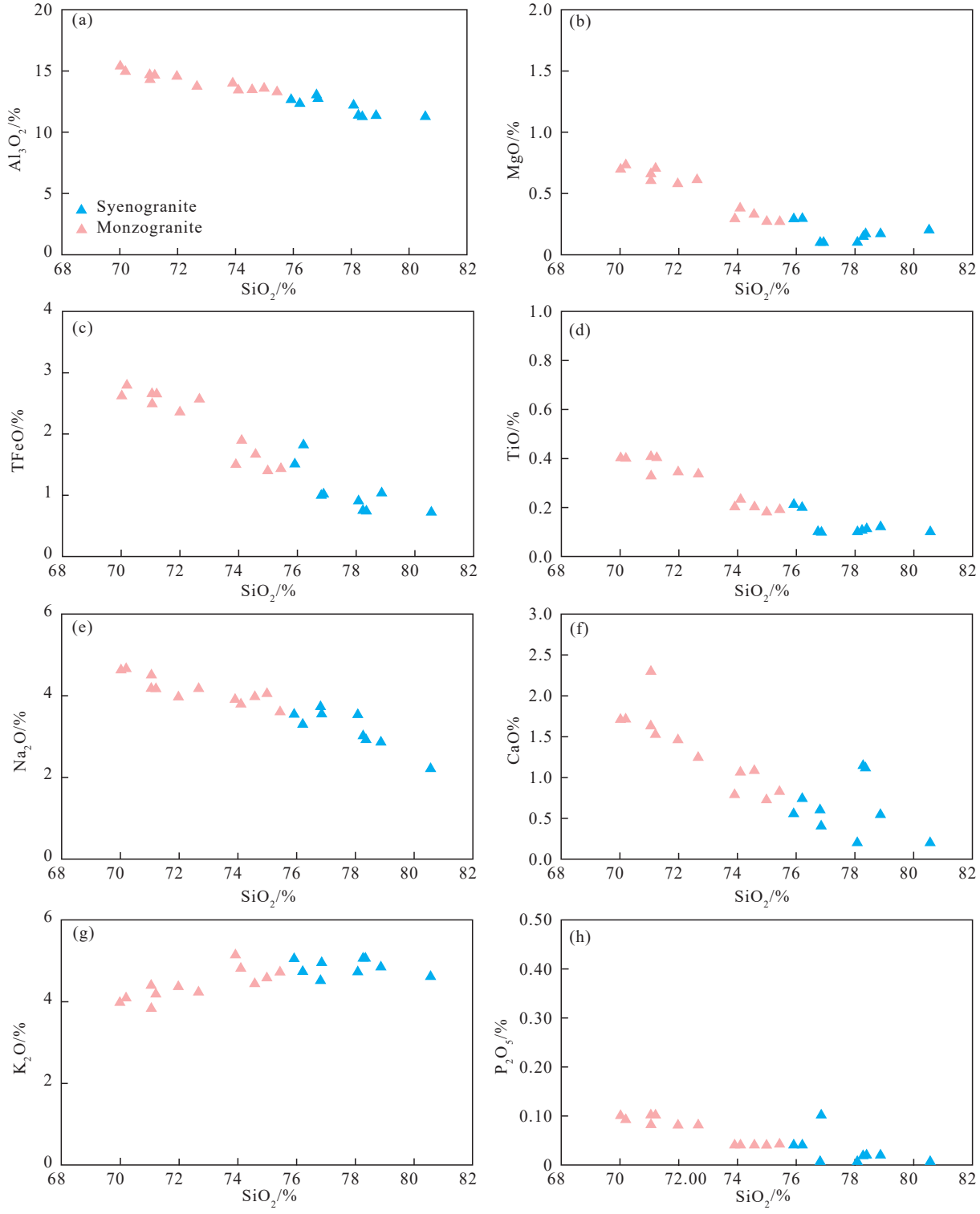

Fig. 12. Harker diagrams showing the magmatic evolution of fine-grained syengranite and coarse-grained monzogranite. Data from Dai M et al. (2022) and Zhai DG et al. (2020).

(Fig. 12), and plot in the opposite direction of fractional crystallization to the coarse-grained monzogranite (Fig. 15), indicating accumulations of plagioclase were left behind during the formation of the fine-grained syenogranite (Sisson TW, 1994). The fine-grained syenogranite has positive Rb and negative Sr and Eu anomalies, which also support crystal fractionation of plagioclase (Fig. 14). The decreasing Fe_2O_3 contents are most likely the results of magnetite fractionation (Fig. 12). Moreover, the fine-grained syenogranite show the Zr/Hf ratios have a negative correlation with δEu values, and the La/Yb and Gd/Yb ratios decrease with the Rb/Sr ratio increase, along with decreasing TiO_2, CaO and P_2O_5 contents, which suggest LREE-rich minerals fractional crystallization (apatite, titanite, and monazite) (Fig. 15). Furthermore, both the fine-grained syenogranite and coarse-grained monzogranite samples show an obvious genetic relationship

Table 6. Major element (%) and trace element (10^{-6}) concentrations of syenogranite and monzogranite in the SJZ Ag-Pb-Zn deposit.

Sample	ZK1237-3	ZK1237-4	ZK1237-8	ZK1237-8R	ZK1237-9	17SJ-47	17SJ-48	17SJ-49	17SJ-50	ZK1237-5	ZK1237-6	ZK1237-7	ZK1237-10	ZK101-1	ZK101-2	ZK101-3	ZK101-4	ZK101-5	17SJ-51	17SJ-52	17SJ-53
	Fine-grained syenogranite									Monzogranite											
SiO_2	74.83	74.99	77.28	77.18	77.97	80.00	77.30	76.20	75.70	69.24	70.92	68.38	71.23	74.95	74.24	73.01	73.05	73.52	69.70	70.00	69.60
TiO_2	0.20	0.21	0.11	0.11	0.12	0.10	0.10	0.10	0.10	0.32	0.34	0.39	0.33	0.19	0.18	0.20	0.23	0.20	0.40	0.40	0.40
Al_2O_3	12.17	12.55	11.20	11.21	11.25	11.20	12.10	12.90	12.60	14.05	14.35	14.57	13.47	13.21	13.45	13.84	13.25	13.28	14.30	14.40	15.30
TFe_2O_3	1.99	1.63	0.83	0.83	1.14	0.80	1.00	1.10	1.10	2.70	2.59	3.03	2.80	1.58	1.54	1.65	2.08	1.83	2.90	2.90	2.90
MnO	0.03	0.03	0.01	0.01	0.01	0.00	0.00	0.00	0.00	0.06	0.04	0.05	0.05	0.04	0.03	0.03	0.04	0.04	0.10	0.10	0.10
MgO	0.29	0.29	0.16	0.15	0.17	0.20	0.10	0.10	0.10	0.64	0.57	0.72	0.60	0.27	0.27	0.29	0.37	0.32	0.60	0.70	0.70
CaO	0.73	0.55	1.12	1.13	0.54	0.20	0.20	0.60	0.40	2.24	1.44	1.67	1.22	0.81	0.72	0.78	1.05	1.07	1.60	1.50	1.70
Na_2O	3.24	3.50	2.92	2.94	2.83	2.20	3.50	3.70	3.50	4.39	3.91	4.54	4.09	3.58	4.01	3.86	3.74	3.92	4.10	4.10	4.60
K_2O	4.67	4.99	4.99	5.01	4.81	4.60	4.70	4.50	4.90	3.72	4.29	3.97	4.15	4.68	4.52	5.09	4.73	4.36	4.30	4.10	4.00
P_2O_5	0.04	0.04	0.02	0.02	0.02	0.00	0.00	0.00	0.10	0.08	0.08	0.09	0.08	0.04	0.04	0.04	0.04	0.04	0.10	0.10	0.10
LOI	2.06	0.86	1.35	1.34	0.88	0.70	0.70	0.70	0.70	2.46	1.50	2.10	1.51	1.10	0.94	1.08	1.13	1.10	1.40	1.40	0.90
TOTAL	100.25	99.64	99.99	99.93	99.74	100.00	99.70	99.90	99.20	99.90	100.03	99.51	99.53	100.45	99.94	99.87	99.71	99.68	99.50	99.70	100.30
$Mg^{\#}$	22.47	26.02	27.63	26.36	22.76	0.33	0.17	0.15	0.15	32.21	30.37	32.27	29.92	25.15	25.70	25.79	26.06	25.73	0.29	0.32	0.32
A/CNK	1.04	1.03	0.91	0.91	1.04	1.25	1.08	1.07	1.07	0.92	1.05	0.98	1.00	1.06	1.05	1.04	1.00	1.01	1.00	1.03	1.02
K_2O/Na_2O	0.69	0.70	0.59	0.59	0.59	0.48	0.74	0.82	0.71	1.18	0.91	1.14	0.99	0.76	0.89	0.76	0.79	0.90	0.95	1.00	1.15
DI	92.04	93.60	94.34	94.42	94.72					84.70	86.69	85.20	87.95	92.06	92.70	92.25	90.50	90.81			
La	23.43	22.46	25.88	26.13	28.54	21.20	24.40	27.10	25.40	25.85	27.32	24.93	25.94	28.79	32.87	46.09	32.09	27.69	30.30	31.40	24.80
Ce	50.30	48.94	53.51	53.96	59.24	9.40	5.90	7.30	8.10	54.60	58.02	53.74	57.27	56.76	64.48	89.45	65.29	57.88	10.40	11.70	11.40
Pr	5.76	5.77	5.87	5.93	6.44	5.30	6.00	6.70	6.20	6.34	6.66	6.32	6.85	6.12	6.78	9.50	7.27	6.55	7.40	7.70	6.60
Nd	21.49	22.06	20.50	20.76	22.54	18.50	21.30	22.90	21.50	24.24	25.00	24.51	26.68	21.31	22.81	29.86	25.78	23.59	27.50	27.70	24.30
Sm	4.78	5.25	4.17	4.18	4.43	4.10	4.70	5.40	4.70	5.29	5.23	5.45	6.06	4.06	4.14	5.09	5.08	4.88	6.20	5.90	5.50
Eu	0.35	0.30	0.22	0.22	0.24	0.20	0.20	0.20	0.20	0.66	0.66	0.71	0.64	0.39	0.40	0.48	0.46	0.45	0.70	0.70	0.60
Gd	4.55	5.06	3.91	3.93	3.99	3.70	4.20	5.20	4.10	4.86	4.67	4.99	5.49	3.55	3.54	4.35	4.40	4.30	5.30	5.10	5.00
Tb	0.81	0.90	0.70	0.71	0.69	0.70	0.70	1.00	0.70	0.81	0.75	0.82	0.91	0.57	0.56	0.68	0.71	0.71	0.90	0.90	0.80
Dy	5.14	5.78	4.55	4.62	4.48	5.00	4.80	6.70	4.90	4.94	4.49	4.96	5.48	3.41	3.43	4.16	4.30	4.38	5.50	5.30	5.40
Ho	1.07	1.21	0.99	1.00	0.96	1.00	0.90	1.40	1.00	1.01	0.89	0.99	1.08	0.69	0.70	0.85	0.87	0.88	1.00	1.00	1.00
Er	3.37	3.81	3.13	3.19	3.11	3.50	3.00	4.70	3.40	3.06	2.63	2.94	3.19	2.11	2.23	2.68	2.67	2.76	3.20	3.10	3.30
Tm	0.56	0.64	0.54	0.54	0.53	0.60	0.50	0.80	0.60	0.50	0.42	0.46	0.50	0.35	0.37	0.45	0.44	0.45	0.50	0.50	0.50
Yb	3.78	4.33	3.64	3.70	3.67	4.20	3.40	5.50	4.00	3.43	2.75	3.01	3.33	2.43	2.73	3.16	3.09	3.18	3.30	3.10	3.30
Lu	0.57	0.65	0.56	0.57	0.57	0.60	0.50	0.80	0.60	0.51	0.42	0.45	0.50	0.38	0.43	0.49	0.48	0.49	0.50	0.50	0.50
$(La/Yb)_N$	4.45	3.72	5.11	5.06	5.57	3.62	5.15	3.53	4.55	5.41	7.12	5.93	5.59	8.50	8.65	10.45	7.46	6.24	6.59	7.27	5.39
$(Gd/Yb)_N$	1.00	0.97	0.89	0.88	0.90	0.73	1.02	0.78	0.85	1.17	1.40	1.37	1.37	1.21	1.07	1.14	1.18	1.12	1.33	1.36	1.25
δEu	0.23	0.18	0.17	0.17	0.17	0.05	0.04	0.04	0.05	0.39	0.40	0.41	0.33	0.31	0.31	0.30	0.29	0.29	0.12	0.13	0.11
ΣREE	125.96	127.17	128.16	129.45	139.43	113.10	111.80	144.10	119.40	136.08	139.92	134.28	143.95	130.91	145.46	197.28	152.91	138.21	134.60	136.30	126.40
Rb	252.19	271.25	240.22	238.35	239.70	250.80	247.50	252.00	276.80	182.01	193.95	182.26	212.19	313.70	300.90	325.73	236.30	240.36	207.40	227.90	214.20

Table 6. (*Continued*).

Sample	ZK123 7-3	ZK123 7-4	ZK123 7-8	ZK123 7-8R	ZK123 7-9	17SJ-47	17SJ-48	17SJ-49	17SJ-50	ZK123 7-5	ZK123 7-6	ZK123 7-7	ZK123 7-10	ZK101-1	ZK101-2	ZK101-3	ZK101-4	ZK101-5	17SJ-51	17SJ-52	17SJ-53
	Fine-grained syenogranite									Monzogranite											
Ba	303.00	283.57	214.11	216.17	241.98	212.70	151.40	152.70	150.30	440.75	477.01	518.12	395.90	287.22	288.18	366.51	340.73	294.51	435.70	457.80	480.50
Th	31.15	34.39	31.09	30.40	34.18	32.40	37.30	38.80	39.40	18.63	24.11	19.32	24.24	36.89	37.57	42.43	41.28	39.49	26.00	22.90	18.00
U	11.22	13.00	11.67	11.44	12.04	12.80	19.10	22.30	15.20	6.60	7.72	6.94	8.54	16.75	19.11	22.41	15.82	17.14	9.00	7.80	6.90
K	39465.39	41917.78	41977.27	42166.89	40373.02	38456.03	39411.10	37657.95	41296.73	31679.07	36128.97	33818.45	35131.78	39088.12	37885.24	42753.49	39814.30	36699.86	36387.76	34624.71	33406.38
Nb	11.96	15.61	8.98	8.97	9.53	12.60	12.90	14.80	15.40	11.12	11.49	13.03	12.43	12.53	12.41	13.52	14.02	13.80	14.00	12.80	13.00
Ta	2.08	2.93	2.03	2.06	2.11	2.20	2.10	2.40	2.60	1.35	1.39	1.47	1.63	2.49	3.17	3.52	2.41	2.54	1.50	1.30	1.50
Sr	76.69	70.56	69.73	69.50	68.50	58.00	54.60	56.10	55.10	193.63	256.55	226.07	162.05	126.82	139.28	150.68	147.52	147.68	262.00	267.50	291.10
P	177.77	176.71	88.48	88.52	88.28	0.00	0.00	0.00	443.03	358.28	354.31	403.19	356.16	175.69	176.32	176.69	177.07	177.07	444.83	443.93	439.02
Zr	128.74	154.66	106.20	107.68	119.05	101.20	105.70	171.20	125.00	156.43	176.15	179.20	184.56	134.21	123.48	149.91	132.61	129.82	207.80	196.10	227.10
Hf	4.96	6.22	4.49	4.62	4.94	4.30	4.40	6.50	5.40	5.11	5.75	5.69	6.12	5.13	4.89	5.54	4.58	4.54	6.90	6.30	6.80
Ti	1220.79	1274.18	668.37	668.71	727.51	603.57	605.40	604.18	608.48	1968.31	2068.19	2399.61	2017.80	1146.21	1089.73	1213.38	1398.36	1215.96	2443.83	2438.86	2411.87
Y	34.31	38.29	34.10	34.52	31.26	35.10	31.30	48.40	34.00	30.59	27.03	30.08	33.58	21.72	22.91	27.33	28.84	29.25	31.90	31.70	33.40

in the Rayleigh fractionation model (Fig. 14). A starting composition plotted within the Rb, Sr, and Eu contents gap was chosen to bracket the range of initial trace element concentrations of the coarse-grained monzogranite and the fine-grained syenogranite. In the Rayleigh fractionation model, the most coarse-grained monzogranite are plotted into the cumulate residual field, and all fine-grained syenogranite within the extracted melts zone (Fig. 13). Therefore, these geochemical characteristics indicate that parental magma of the fine-grained syenogranite is extracted from a monzogranite crystal mush (monzogranite).

6.5. Implications for melt extraction and mineralization

As discussed above, the diagenesis of the syenogranite has a close relationship with the ore-forming fluid in the SJZ Ag-Pb-Zn deposit, and the syenogranite was residual melts extracted from the monzogranite crystal mush. Thus, the ore-forming fluid/material originated from the parent magma which the syenogranite and the monzogranite derived. The Sr-Nd-Hf isotopic compositions of the syenogranite and the monzogranite, suggest they originated from partial melting of the juvenile lower-crustal basaltic rocks (Dai M et al., 2022; Ruan BX et al., 2015). Combing with the absence of coeval mafic magmatism rock in the SGHR and most microgranular enclaves (MEs) in the Early Cretaceous granitoids are charactered by high SiO_2 (56.16%–63.70%) content and low $Mg^{\#}$ value (27.72–39.87) (Dai M et al., 2022, Wei W et al., 2020), implying mantle material was not involved in the Early Cretaceous magmatism. Thus, the mantle characters of the SJZ sulfides He-Pb isotopic compositions could be originated from the juvenile lower-crustal basaltic rocks. Ouyang HG et al. (2015) suggested that the upwelling asthenosphere triggered the SGHR Early Cretaceous granitic magmatism. The upwelling asthenosphere heats the lower crust material, which is leading to the large-scale dehydration melting of lower crust materials and the dehydration of lower crust material would generate a large amount of fluid (gas-liquid phase) (Zhang Q, 2012). The metal elements could be extracted by those fluids from the lower crust materials because these fluids have relatively high activity and the metal elements have a low value of $D^{melt/fluid}$ and $D^{crystal/fluid}$ (Luo ZH et al., 2011).

The mixing/mingling between the fluids and the intermediate-acid magma of the monzogranite would greatly increase the fluidity of the intermediate-acid magma (Luo ZH et al., 2010). Then, these fertilized fluids mixing/mingling with the parent magma of the monzogranite and underplating to the upper crust. The monzogranite is a coarse-grained structure, indicating the monzogranite magma underwent cooling crystallization and homogenization, then formed an inactive crystal mush. These fertilized fluids were trapped in the intergranular melt, which is an unfavorable condition for mineralization (Luo ZH et al., 2010, 2014, Zhang SH, 2011).

The MEs have been observed in the monzogranite and the MEs have similar zircon U-Pb age and Hf isotopic with the

monzogranite (Dai M et al., 2022), implying that the magma recharge has triggered the melt extraction and crystal-melt segregation processes in the SJZ Ag-Pb-Zn deposit. The injected less-felsic magmas from deeper crustal levels are typically hotter than the shallow silicic crystal mush they intrude, which can provide very large amounts of thermal energy to decrease magma viscosity (Luo ZH et al., 2014). Furthermore, the fluids also have been recharged from deeper magma reservoirs. Then, the fertilized fluids and intergranular melt (syenogranite magma) are extracted from the crystal mush and emplaced in the shallow. The melt extraction further concentrated the fertilized fluids, which were dispersed in the magma chamber. Because P-T conditions sharply changed in the shallow, the syenogranite magma rapid cooling crystallization and decoupled with the fertilized fluids. The fertilized fluids mixed with meteoric waters, which led to the mineralization in the SJZ Ag-Pb-Zn deposit.

Collectively, a four-stage model for formation of the ore-forming fluid in the SJZ Ag-Pb-Zn deposit have been proposed (Fig. 16), which is including (1) the primary fluids

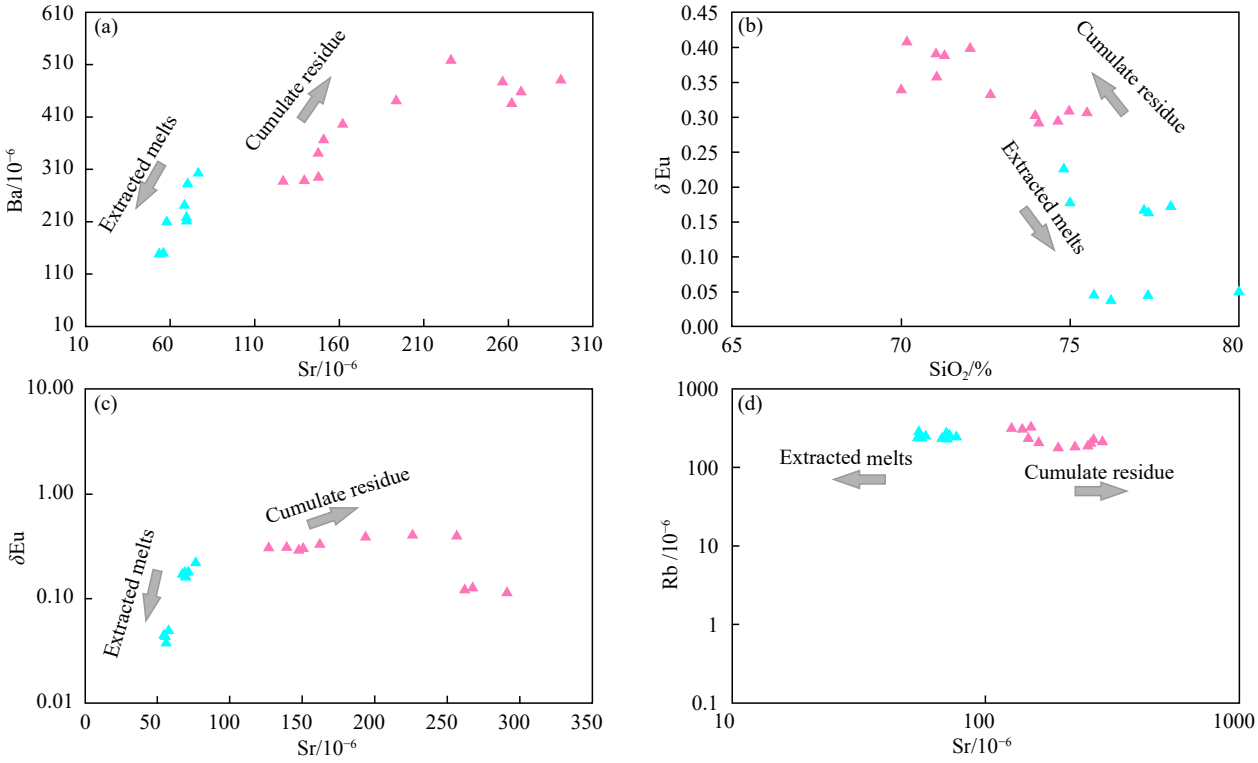

Fig. 13. Co-variations of element concentrations and elemental ratios of the fine-grained syengranite and coarse-grained monzogranite. a–Ba *vs.* Sr; b–*d*Eu *vs.* SiO_2 ; c–*d*Eu *vs.* Sr; and d–Rb *vs.* Sr. The symbols are the same as in Fig. 12.

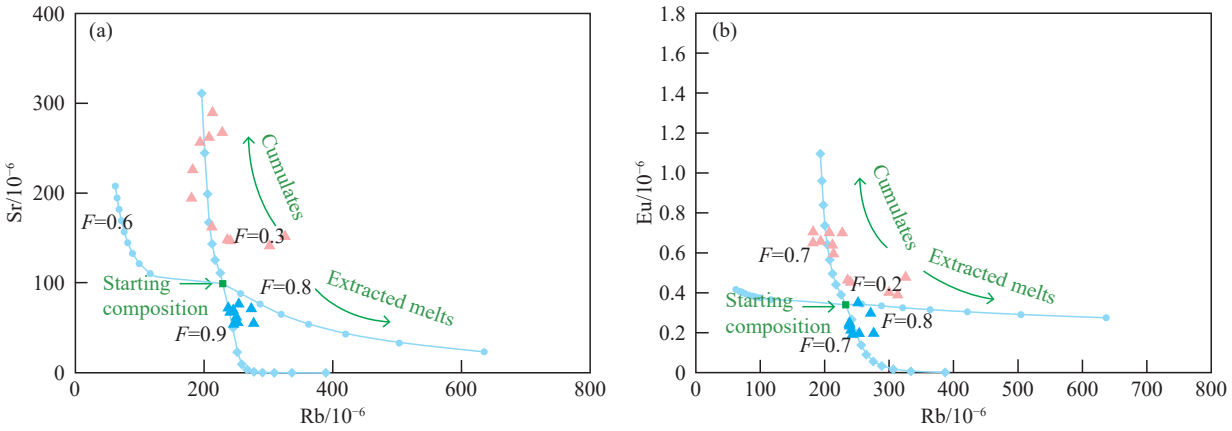

Fig. 14. Trace element modeling obtained using Sr *vs.* Rb (a) and Eu *vs.* Rb (b) diagrams. Fractionating mineral assemblage resembles that in the Shuangjianzishan monzogranite. Starting compositions (Rb=240×10^{-6}; Sr=100×10^{-6}; Eu=0.35×10^{-6}) have been considered to plot within the compositional gap (see text for further information). Complementary fractional crystallization models use the same starting composition tracking evolution of melt, and the cumulate crystallized from that melt. Partition coefficients have been estimated based on the assumed mineral proportions of the Shuangjianzishan monzogranite (25% quartz, 38% plagioclase, 30% alkali-feldspar, 5% biotite, 1% hornblende, 1% accessory minerals). Symbols and numbers along the lines indicate melt fraction (F). High and low partition coefficients have been tested (Appendix S1). Partition coefficients are listed in Appendix S1. Symbols are the same as in Fig. 12.

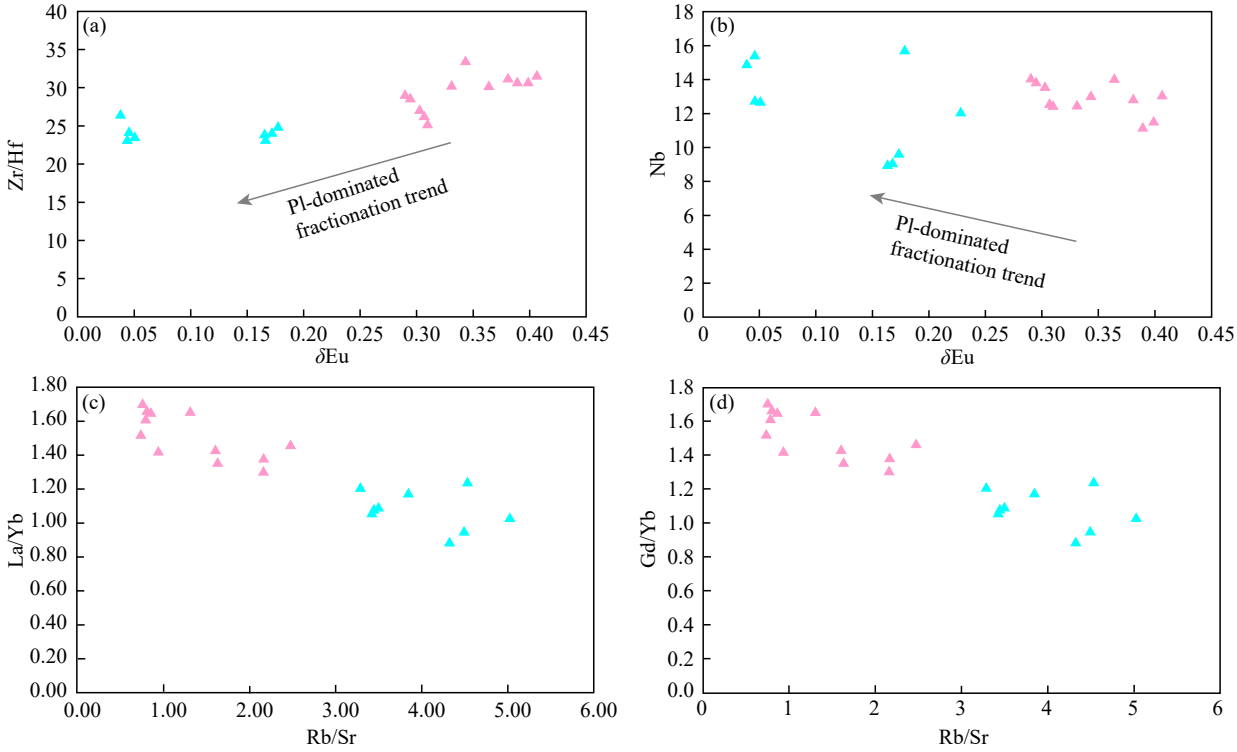

Fig. 15. Trace element geochemistry of the fine-grained syengranite and coarse-grained monzogranite. a–Zr/Hf *vs.* *d*Eu; b–Nb *vs.* *d*Eu; c–La/Yb *vs.* Rb/Sr; d–Gd/Yb *vs.* Rb/Sr. The symbols are the same as in Fig. 12.

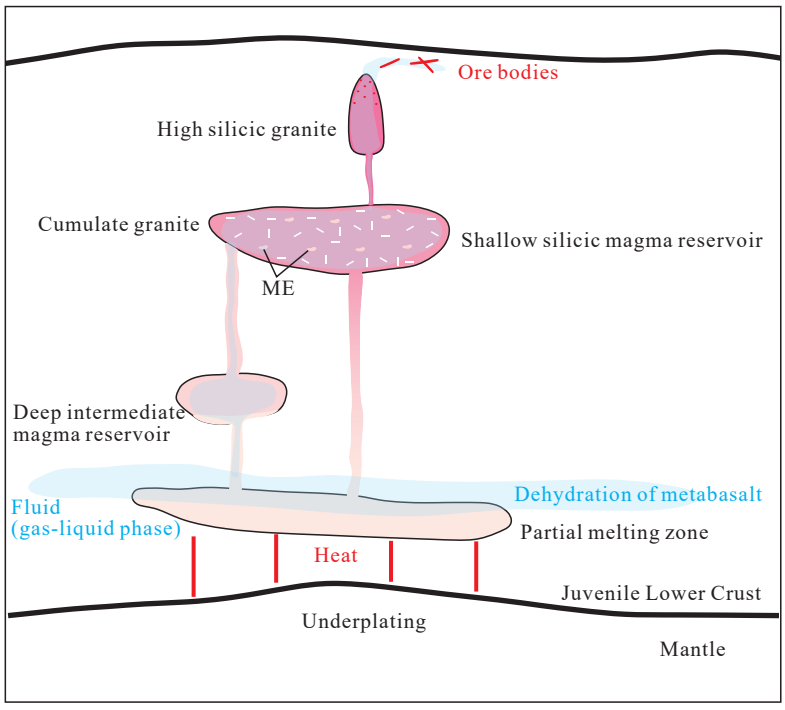

Fig. 16. Diagrammatical model illustrating the origin of the causative intrusion and ore-forming fluid (modified from Dai M et al., 2022).

(gas-liquid phase) origin from large-scale dehydration and partial melting of the juvenile lower crust metabasaltic rock, and the metal elements extracted by the fluids metasomatism from lower crust; (2) these fertilized fluids migrated with the underplating parent magma of the monzogranite, and the fertilized fluid was trapped in intergranular melt in the upper crust magma reservoirs; (3) the fertilized fluids and intergranular melt extracted from the crystal mush, which is triggered by the recharging of the less felsic magma from deep magma reservoirs; (4) the intergranular silicic melts underwent rapid cooling crystallization and decoupled with the fluids in the shallow part of the crust, then these fertilized fluids mixed with meteoric waters and interacted with wall-rocks which leading to the mineralization in the SJZ Ag-Pb-

Zn deposit.

7. Conclusions

Based on geology, mineralogy, whole-rock geochemical data, *in-situ* S-Pb isotope data, and bulk Pb-C-O-He-Ar isotope data of the SJZ Ag-Pb-Zn deposit, it can draw the following conclusions:

(i) The syenogranite is the causative intrusion of the SJZ Ag-Pb-Zn deposit, the mantle-derived features of the SJZ ore-forming fluids might be caused by the parent magma of the syenogranite, which derived form partial melting of the juvenile lower crust.

(ii) The syenogranite melt extracted from the crystal mush was critical to the mineralization of the SJZ Ag-Pb-Zn deposit, which effectively concentrated the fertilized fluids from a homogeneous magma reservoir.

(iii) A four-stage model includes: (1) The generation of the ore-forming fluids was caused by large-scale partial melting of a juvenile lower crust; (2) the fertilized fluids trapped by intergranular melt in the upper crust magma reservoirs; (3) the fertilized fluids and the intergranular melt extracted from the crystal mush; (4) the intergranular silica melt decoupled with the fluids, and the fertilized fluids mixed with meteoric waters which lead to the mineralization in the SJZ Ag-Pb-Zn deposit.

CRediT authorship contribution statement

Meng Dai, Guang-sheng Yan, Yong-sheng Li, Wen-bin Jia, Fan-yu Qi, Xing Ju conceived of the presented idea. Meng Dai and Wen-bin Jia carried out the experiment. All authors discussed the results and contributed to the final manuscript.

Declaration of competing interest

The authors declare no conflicts of interest.

Acknowledgment

The authors thank Dr. Lu Chen and Dr. Min Liu (Northwest University) for *in-situ* S and Pb isotope analyses, Chun-lei Zong (Northwest University) and Li Liu for bulk rock Pb isotope analyses, Biao Yang for sample preparations. Dr. Hai-rui Sun, Dr. Kui-feng Mi (China Geological Survey), and Prof. De-gao Zhai (China University of Geosciences) are thanked for their suggestions on the early version of the manuscript. This research was supported financially by the China Geological Survey project [DD20160123 (DD-16-049, D1522), DD20160050, DD20190370], the Fundamental Research Funds for the Central Universities (310827171122), the National Natural Science Foundation of China (Grant 41672068).

Supplementary dataset

Supplementary data to this article can be found online at doi: 10.31035/cg2022044.

References

Andrew A, Godwin CI, Sinclair AJ. 1984. Mixing line isochrons: A new interpretation of galena lead isotope data from Southeastern British Columbia. Economic Geology, 79, 919–932. doi: 10.2113/gsecongeo.79.5.919.

Baker T, Achterberg VE, Ryan GC, Lang RJ. 2004. Composition and evolution of ore fluids in a magmatic-hydrothermal skarn deposit. Geological Society of America, 32, 117–120.

Bao ZA, Yuan WT, Yuan HL, Liu X, Chen KY, Zong CL. 2016a. Non-matrix-matched determination of lead isotope ratios in ancient bronze artifacts by femtosecond laser ablation multi-collector inductively coupled plasma mass spectrometry. International Journal of Mass Spectrometry, 402, 12–19. doi: 10.1016/j.ijms.2016.03.001.

Bao ZA, Yuan HL, Zong CL, Liu Y, Chen KY, Zhang YL. 2016b. simultaneous determination of trace elements and lead isotopes in fused silicate rock powders using a boron nitride vessel and fsLA-(MC)-ICP-MS. Journal of Analytical Atomic Spectrometry, 31, 1012–1022. doi: 10.1039/C5JA00410A.

Barton PB, Bethke PM. 1987. Chalcopyrite disease in sphalerite: Pathology and epidemiology. American Mineralogist, 72 (5–6), 451–467.

Beane R, Wiebe RA. 2012. Origin of quartz clusters in Vinalhaven granite and porphyry, coastal Maine. Contributions to Mineralogy and Petrology, 163(6), 1069–1082. doi: 10.1007/s00410-011-0717-1.

Cai HA, Yang ZA, Yin ZW, Xiao WJ, Li YY. 2021. Metallogenic regularity and exploration direction of Shuangjianzishan Ag-Pb-Zn deposit in Inner Mongolia, China. Mineral Exploration, 7(12), 1576–1581 (in Chinese with English abstract).

Clayton RN, Mayeda TK. 1963. The use of bromine pentafluoride in the extraction of oxygen from oxides and silicates for isotopic analysis. Geochimica et Cosmochimica Acta, 27, 43–52. doi: 10.1016/0016-7037(63)90071-1.

Chen L, Chen KY, Bao ZA, Liang P, Sun TT, Yuan HL. 2016. Preparation of standards for in situ sulfur isotope measurement in sulfides using femtosecond laser ablation MC-ICP-MS. Journal of Analytical Atomic Spectrometry, 32, 107–116. doi: 10.1039/c6ja00270f.

Chiaradia M, Konopelko D, Seltmann R, Cliff AR. 2006. Lead isotope variations across terrane boundaries of the Tien Shan and Chinese Altay. Mineralium Deposita, 41(5), 411–428. doi: 10.1007/s00126-006-0070-x.

Clark I, Fritz P. 1997. Environmental Isotopes in Hydrogeology. New York, Lewis Publishers, 328.

Cook NJ, Ciobanu CL, Pring A, Skinner W, Shimizu M, Danyushevsky L, Saini-Eidukat B, Melcher F. 2009. Trace and minor elements in sphalerite: A LA-ICP-MS study. Geochimica et Cosmochimica Acta, 73, 4761–4791. doi: 10.1016/j.gca.2009.05.045.

Cooke DR, Deyell CL, Waters PJ, Gonzales RI, Zaw K. 2011. Giant porphyry deposits: Characteristics, distribution, and tectonic controls. Economic Geology, 100(5), 801–818. doi: 10.2113/gsecongeo.100.5.801.

Craig H. 1961. Isotopic variations in meteoric waters. Science, 133(3465), 702–1703.

Dai M, Yan GS, Liu C, Deng JF, Li YS, Jia WB, Lai CK. 2019. Southward subduction of the Mongolia–Okhostk Ocean: Insights from Early–Middle Triassic intrusive rocks from the Jiawula–Tsagenbulagen area in NE China. Geological Journal, 55(1),

1–27. doi: 10.1002/gj.3435.

Dai M, Yan GS, Li YS, Gong, FY, Jia WB. 2022. The origin of microgranular enclaves in the Early Cretaceous Shuangjianzishan granites in southern Great Hinggan Range, NE China. Geological Journal. doi: 10.1002/gj.4432.

Doe BR, Zartman RE. 1979. Plumbotectonics, the phanerozoic. Geochemistry of Hydrothermal Ore deposits. New York, Wiley Interscience Publications, 22–70.

Eldridge CS, Bourcier WL, Ohmoto H, Barnes HL. 1988. Hydrothermal inoculation and incubation of the chalcopyrite disease in sphalerite. Economic Geology, 83(5), 978–989. doi: 10.2113/gsecongeo.83.5.978.

Jahn BM, Wu F, Chen B. 2000. Granitoids of the Central Asian orogenic belt and continental growth in the Phanerozoic. Geological Society of America, Special Papers, 350, 181–193.

Jiang B, Wang DH, Chen YC, Zhang T, Pu XL, Ma WW, Wang Y, Wu G, Wu LW, Zhang T, Li XJ, Yan J, Zuo YS, Sun HJ, Li ZY. 2022. Classification, metallogenesis and exploration of silver deposits in Daxing 'anling of Inner Mongolia and its adjacent areas. China Geology. doi: 10.31035/cg2022005.

Jiang SH, Nie FJ, Liu YF, Yun, F. 2010. Sulfur and lead isotopic compositions of Bairendaba and Weilasituo silver-polymetallic deposits, Inner Mongolia. Mineral Deposits, 29(1), 101–112 (in Chinese with English abstract).

Jiang SH, Nie FJ, Bai DM, Niu SY, Wang BD, Liu YF, Liu Y. 2011a. Study on the lead isotopic features of the Baiyinnuoer Pb-Zn deposit in Inner Mongolia. Journal of Earch Sciences and Environment, 33, 230–238 (in Chinese with English abstract).

Jiang SH, Nie FJ, Bai DM, Liu YF, Liu Y. 2011b. Geochronology evidence for Indosinian mineralization in Baiyinnuoer Pb-Zn deposit of Inner Mongolia. Mineral Deposits, 30, 787–798 (in Chinese with English abstract).

Jiang SH, Chen CL, Bagas L, Liu Y, Han N, Kang H, Wang ZH. 2017. Two mineralization events in the Baiyinnuoer Zn-Pb deposit in Inner Mongolia, China: Evidence from field observations, S-Pb isotopic compositions and U-Pb zircon ages. Journal of Asian Earth Sciences, 144, 339–367. doi: 10.1016/j.jseaes.2016.12.042.

Kendrick MA, Burgess, R, Pattrick, RAD, Turner, G. 2001. Fluid inclusion noble gas and halogen evidence on the origin of Cu-porphyry mineralizing fluids. Geochimica et Cosmochimica Acta, 65, 2651–2668. doi: 10.1016/S0016-7037(01)00618-4.

Kendrick MA, Burnard P. 2013. Noble gases and halogens in fluid inclusions: A journey through the Earth's Crust. The Noble Gases as Geochemical Tracers, 319–369.

Kuang YS., Zheng GR, Lu MJ, Liu YL, Zhang SJ, Li Y, Chen WJ. 2014. Basic characteristics of Shuangjianzishan sliver polymetallic deposit in Chifeng City, Inner Mongolia. Mineral Deposits, 33(4), 847–856 (in Chinese with English abstract).

Li JF, Wang KY, Quan HY, Sun FY, Zhao LS, Zhang XB. 2016. Discussion on the magmatic evolution sequence and metallogenic geodynamical setting background Hongling Pb-Zn deposit in the southern Da Xing 'an Mountains. Acta Petrologica Sinica, 32(5), 1529–1542.

Li JY, Qian Y, Tekoumc L, Zhao CJ, Sun JL, Zheng T, Sun FY, Shen YJ. 2021. Petrogenesis of Jurassic Granitoids on Liaodong Peninsula, Northeast China: Constraints on the Evolution of the Mongol-Okhotsk and Pacific Tectonic Regimes. Journal of Earth Science, 32(1), 127–143. doi: 10.1007/s12583-020-1372-0.

Liu C, Deng JF, Xu LQ, Zhang Y, Zhao HD, Kong WQ, Li N, Luo ZH, Bai LB, Zhao, GC, Su SG. 2011. A preliminary frame of magma-tectonic-Mo metallogenic events of Mesozoic era in Da Hingganmountains and Xiao Hinggan mountains areas. Earth Science Fronters, 18, 166–178 (in Chinese with English abstract).

Liu HB, Jin GS, LI JJ, Han J, Zhang JF, Zhang J, Zhong FW, Guo DQ. 2013. Determination of stable isotope composition in uranium geological samples. World Nuclear Geoscience, 30(3), 174–179 (in Chinese with English abstract).

Liu YF, Jiang S, Bagas L. 2016. The genesis of metal zonation in theWeilasituo and Bairendaba Ag-Zn-Pb-Cu-(Sn-W) deposits in the shallowpart of a porphyry Sn-W-Rb system, Inner Mongolia, China. Ore Geology Review, 75, 150–173. doi: 10.1016/j.oregeorev.2015.12.006.

Liu YF, Jiang S, Bagas L, Han N, Chen CL, Kang H. 2017. Isotopic (C-O-S) geochemistry and Re-Os geochronology of the Haobugao Zn-Fe deposit in Inner Mongolia, NE China. Ore Geology Review, 82, 130–147. doi: 10.1016/j.oregeorev.2016.11.024.

Liu LJ, Zhou, TF, Zhang DY, Yuan F, Liu G. X, Zhao ZC, Sun JD, White N. 2018. S isotopic geochemistry, zircon and cassiterite U-Pb geochronology of the Haobugao Sn polymetallic deposit, southern Great Xing'an Range, NE China. Ore Geology Review, 93, 168–180. doi: 10.1016/j.oregeorev.2017.12.008.

Luo ZH, Lu XX, Xu JY, Liu C and Li DD. 2010. Petrographic indicators of the ore-bearing intrusions. Acta Petrologica Sinica, 26(8): 2247–2254 (in Chinese with English abstrac). doi: CNKI:SUN:YSXB.0.2010-08-003.

Luo ZH, Lu XX, Liu C, Li DD, Yang ZZ, Wen SB. 2011. On failing of the magmatic hydrothermal metallogenic theory: The causes and new departure. Journal of Jilin University (Earth Science Edition), 41(1), 1–11 (in Chinese with English abstract).

Luo ZH, Zhou JL, Hei HX, Liu C, Su SG. 2014. Post – supereruption – superintrusion) metallogenesis. Acta Petrologica Sinica, 30(11), 3131–3154 (in Chinese with English abstract).

Mao JW, Xie GQ, Zhang ZH, Li XF, Wang YT, Zhang CQ, Li YF. 2005. Mesozoic large-scale metallogenic pulses in North China and corresponding geodynamic settings. Acta Petrologic Sinica, 21, 169–188 (in Chinese with English abstract).

Mamyrin BA, Tolstikhin LN. 1984. Helium isotopes in nature developments in geochemistry. Amsterdam, Elsevier press, 1–273.

Mei W, Lv XB, Liu Z, Tang RK, Ai ZL, Wang XD, Cisse M. 2015. Geochronological and geochemical constraints on the ore-related granites in Huanggang deposit, Southern Great Xing'an Range, NE China and its tectonic significance. Geosciences Journal, 19(1), 53–67. doi: 10.1007/s12303-014-0021-y.

Meinert LD, Dipple GM, Nicolescu S. 2005, World skarn deposits. Economic Geology 100th Anniversary Volume, 299–336.

Nie FJ, Jiang SH, Zhang Y, Bai DM, Hu P, Zhao YY, Zhang WY, Liu Y. 2007. Metallogenic Studies and Prospecting Orientation in Central and Eastern Segments along China-Mongolia Border. Beijing, Geological Publishing House, 574 (in Chinese with English abstract).

Niu SY, Sun AQ, Guo LJ, Wang BD, Hu HB, Jian M. 2008. Ore-control structures and prospecting for the Baiyinnuoer Pb-Zn deposit in the Da Hinggan range. Geotectonica Et Metallogenia, 32, 72–80 (in Chinese with English abstract).

Ohmoto H. 1972. Systematics of sulfur and carbon isotopes in hydrothermal ore deposits. Economic Geology. 67 (5), 551–578. doi: 10.2113/gsecongeo.67.5.551.

Ohmoto H, Rye R. 1979. Isotopes of sulfur and carbon. In: Barnes HL (ed.), Geochemistry of Hydrothermal Ore Deposits. New York, John Wiley and Sons Inc press, 509–567.

Ouyang HG, Mao JW, Santosh M, Wu Y, Hou L, Wang XF. 2014. The

Early Cretaceous Weilasituo Zn-Cu-Ag vein deposit in the southern Great Xing'an Range, northeast China: Fluid inclusions, H, O, S, Pb isotope geochemistry and genetic implications. Ore Geology Review, 56, 503–515. doi: 10.1016/j.oregeorev.2013.06.015.

Ouyang HG, Mao JW, Zhou ZH, Su HM. 2015. Late Mesozoic metallogeny and intracontinental magmatism, southern Great Xing' an Range, northeastern China. Gondwana Research, 27, 1153–1172. doi: 10.1016/j.gr.2014.08.010.

Rollinson H. 1993. Using geochemical data: London. Longman, 352.

Ruan BX, Lv XB, Yang W, Liu ST, Yu YM, Wu CM. 2015. Geology, geochemistry and fluid inclusions of the Bianjiadayuan Pb-Zn-Ag deposit, Inner Mongolia, NE China: Implications for tectonic setting and metallogeny. Ore Geology Reviews, 121–137. doi: 10.1016/j.oregeorev.2015.05.004.

Seal RR. 2006. Sulfur isotope geochemistry of sulfide minerals. Reviews in Mineralogy and Geochemistry, 61, 633–677. doi: 10.2138/rmg.2006.61.12.

Sengör AMC, Natal'in BA. 1996. Palaeotectonics of Asia. Fragments of A Synthesis. In: Yin A, Harrison M (Eds.), The Tectonic Evolution of Asia. Rubey Colloquium. Cambridge, Cambridge University Press, 486–640.

Sisson TW. 1994. Hornblende-melt trace-element partitioning measured by ion microprobe. Chemical Geology, 117, 331–344. doi: 10.1016/0009-2541(94)90135-X.

Schaen AJ, Singer BS, Cottle JM, Garibaldi N, Schoene B, Satkoski AM, Fournelle J. 2018. Textural and mineralogical record of low-pressure melt extraction and silicic cumulate formation in the late Miocene Risco Bayo–Huemul plutonic complex, southern Andes. Journal of Petrology, 59, 1991–2016. doi: 10.1093/petrology/egy087.

Shen P, Hattori K, Pan H, Jackson S, Seitmuratova E. 2015. Oxidation condition and metal fertility of granitic magmas: Zircon trace-element data from porphyry Cu deposits in the Central Asian orogenic belt. Economic Geology, 110(7), 1861–1878. doi: 10.2113/econgeo.110.7.1861.

Shu QH, Lai Y, Wang C, Meng S. 2013. Ore genesis and hydrothermal evolution of the Baiyinnuo 'er Zinc-Lead skarn deposit, Northeast China: Evidence from isotopes (S, Pb) and fluid inclusions. Economic Geology, 108, 835–860. doi: 10.2113/econgeo.108.4.835.

Stuart FM, Turner G, Duckworth RC, Fallick AE. 1994. Helium isotopes as tracers of trapped hydrothermal fluids in ocean-floor sulfides. Geology, 22(9), 823–826. doi: 10.1130/0091-7613(1994)022<0823:HIATOT>2.3.CO;2.

Taylor HP. 1974. The application of oxygen and hydrogen isotope studies to problems of hydrothermal alteration and ore deposition. Economic Geology, 68(7), 843–883.

Taylor HP, Frechen J, Degens ET. 1967. Oxygen and carbon isotope studies of carbonatites from the Laacher See District, West Germany and the Alnö District. Sweden, Geochimica et Cosmochimica Acta, 31(3), 407–430. doi: 10.1016/0016-7037(67)90051-8.

Tolstikhin IN. 1978. A review: Some recent advances in isotope geochemistry of light rare gases. In: Alexander EC, Ozima M (Eds.), Terrestrial Rare Gases. Tokyo, Japan Scientific Society Press, 27–62.

Vernon RH, Collins WJ. 2011. Structural criteria for identifying granitic cumulates. Journal of Geology, 119(2), 127–142. doi: 10.1086/658198.

Wang XD, Xu DM, Lv XB, Wei W, Mei W, Fan XJ, Su BK. 2018. Origin of the Haobugao skarn Fe-Zn polymetallic deposit, Southern Greatxing'an range, NE China: Geochronological, geochemical, and Sr-Nd-Pb isotopic constraints. Ore Geology Reviews. 94, 58–72. doi: 10.1016/j.oregeorev.2018.01.022.

Wei W, Chen JP, Huang XK, Zhu XY, Xu Q, Liu Z. 2017. Magmaticmigmatization of Haliheiba pluton: Petrographicstudy of dark inclusion, U—Pb chronology and Hfisotopeofzircon mineral in centraland southern section of the Da Hinggan M ountainsarea. Mineral Exploration, 8(6). 948–956 (in Chinese with English abstract). DOI: 10.3969/j.issn.1674-7801.2017.06.005.

Wei W, Zou T, Huang XK, Jiang BB, Zhu XY, Wu XY. 2020. Petrogenesis of Early Cretaceous granitoids in the southern Great Xing 'an Range, NE China: constraints from the Haliheiba pluton.Geochemistry, 80(2): 125608. doi: 10.1016/j.chemer.2020.125608.

Wu FY, Wilde SA, Sun DY, Zhang G. 2004. Geochronology and petrogenesis of post-orogenic Cu, Ni-bearing mafic–ultramafic intrusions in Jilin, NE China. Journal of Asian Earth Sciences, 23, 781–797. doi: 10.1016/S1367-9120(03)00114-7.

Wu FY, Sun DY, Ge WC, Zhang YB, Grant ML, Wilde SA, Jahn BM. 2011, Geochronology of the Phanerozoic granitoids in northeastern China. Journal of Asian Earth Sciences, 41(1), 1–30. doi: 10.1016/j.jseaes.2010.11.014.

Xu B, Charvet J, Chen Y, Zhao P, Shi G. 2012. Middle Paleozoic convergent orogenic belts in western Inner Mongolia (China): Framework, kinematics, geochronology and implications for tectonic evolution of the Central Asian Orogenic Belt. Gondwana Research, 23(4), 1342–1364. doi: 10.1016/j.gr.2012.05.015.

Xu WL, Wang F, Pei FP, Meng E. 2013. Mesozoic tectonic regimes and regional ore-forming background in NE China, constraints from spatial and temporal variations of Mesozoic volcanic rock associations. Acta Petrologica Sinica, 29(2), 339–353 (in Chinese with English abstract).

Xu B, Zhao P, Wang Y, Liao W, Luo Z, Bao Q, Zhou Y. 2015. The pre-Devonian tectonic framework of Xing 'an–Mongolia orogenic belt (XMOB) in north China. Journal of Asian Earth Sciences, 97, 183–196. doi: 10.1016/j.jseaes.2014.07.020.

Xiao WJ, Windley BF, Huang BC, Han CM, Yuan C, Chen HL, Sun M, Sun S, Li JL. 2009. End-Permian to mid-Triassic termination of the accretionary processes of the southern Altaids: Implications for the geodynamic evolution, Phanerozoic continental growth, and metallogeny of Central Asia. International Journal of Earth Sciences, 98(6), 1189–1217. doi: 10.1007/s00531-008-0407-z.

Yang H, Ma WL, Wang R, Ma XL, Wang KY. 2020. Factors Controlling Deposition of Metallic Minerals in the Meng 'entaolegai Ag-Pb-Zn Deposit, Inner Mongolia, China: Evidence from Fluid Inclusions, Isotope Systematics, and Thermodynamic Model. Journal of Earth Science, 31(2), 271–286. doi: 10.1007/s12583-019-1273-2.

Ye L, Cook NJ, Ciobanu, CL, Liu YP, Zhang Q, Liu TG, Gao, W, Yang YL, Danyushevsky L. 2011. Trace and minor elements in sphalerite from basemetal deposits in South China: A LA-ICPMS study. Ore Geology Review., 39, 188–217. doi: 10.1016/j.oregeorev.2021.104663.

Yuan HL, Yin C, Liu X, Chen KY, Bao ZA, Zong CL, Dai MN, Lai SC, Wang R, Jiang SY. 2015. High precision in-situ Pb isotopic analysis of sulfide minerals by femtosecond laser ablation multi-collector inductively coupled plasma mass spectrometry. Science China (Earth Sciences), 58, 1713–1721. doi: 10.1007/s11430-015-5095-5.

Yuan HL, Yuan WT, Cheng C, Liang P, Liu X, Dai M N, Bao Z A, Zong C L, Chen KY, Lai SC. 2016. Evaluation of lead isotope compositions of NIST NBS 981 measured by thermal ionization mass spectrometer and multiple-collector inductively coupled plasma mass spectrometer. Solid Earth Sciences, 1(2), 74–78. doi: 10.1016/j.sesci.2016.04.001.

Zartman RE, Doe BR. 1981. Plumbo tectonics–the model. Tectonophysics, 75, 135–162. doi: 10.1016/0040-1951(81)90213-4.

Zhai DG, Liu JJ, Zhang HY, Yao MJ, Wang JP, Yang YQ. 2014. S-Pb isotopic geochemistry, U-Pb and Re-Os geochronology of the Huanggangliang Fe-Sn deposit, Inner Mongolia, NE China. Ore Geology Review, 59, 109–122. doi: 10.1016/j.oregeorev.2013.12.005.

Zhai DG, Liu JJ, Zhang AL, Sun YQ. 2017. U-Pb, Re-Os, and $^{40}Ar/^{39}Ar$ geochronology of porphyry Sn ± Cu ± Mo and polymetallic (Ag-Pb-Zn-Cu) vein mineralization at Bianjiadayuan, Inner Mongolia, Northeast China: Implications for discrete mineralization events. Economic Geology, 112(8), 2041–2059. doi: 10.5382/econgeo.2017.4540.

Zhai DG, Liu JJ, Zhang HY, Tombros S, Zhang AL. 2018a. A magmatic-hydrothermal origin for Ag-Pb-Zn vein formation at the Bianjiadayuan deposit, Inner Mongolia, NE China: Evidences from fluid inclusion, stable (C-H-O) and noble gas isotope studies. Ore Geology Reviews, 101, 1–16. doi: 10.1016/j.oregeorev.2018.07.005.

Zhai DG, Liu JJ, Cook NJ, Wang XL, Yang YQ. 2019a. Mineralogical, textural, sulfur and lead isotope constraints on the origin of Ag-Pb-Zn mineralization at Bianjiadayuan, Inner Mongolia, NE China. Mineraliu Deposita, 54(1), 47–66. doi: 10.1007/s00126-018-0804-6.

Zhai DG, Bindi L, Voudouris CP, Liu JJ, Tombros FS, Li K. 2019b. Discovery of Se-rich canfieldite, $Ag_8Sn(S, Se)_6$, from the Shuangjianzishan Ag-Pb-Zn deposit, NE China: A multimethodic chemical and structural study. Mineralogical Magazine, 83(3), 419–426. doi: 10.1180/mgm.2018.158.

Zhai DG, Williams-Jones AE, Liu JJ, Selby D, Sun HJ. 2020. The Genesis of the giant Shuangjianzishan epithermal Ag-Pb-Zn deposit, Inner Mongolia, Northeastern China. Economic Geology, 115(1), 101–128. doi: 10.5382/econgeo.4695.

Zhang JH, Gao S, Ge WC, Wu FY, Yang JH, Wilde SA, Li M. 2010. Geochronology of the Mesozoic volcanic rocks in the Great Xing'an Range, northeastern China: Implications for subduction-induced delamination. Chemical Geology, 276, 144–165. doi: 10.1016/j.chemgeo.2010.05.013.

Zhang Q. 2012. Comment on the popular magmatic hydrothermal mineralization theory. Gansu Geology, 21(4), 1–14 (in Chinese with English abstract).

Zhang HY, Zhai DG, Liu JJ, Li PL, Li K, Sun HJ. 2019. Fluid inclusion and stable (H-O-C) isotope studies of the giant Shuangjianzishan epithermal Ag-Pb-Zn deposit, Inner Mongolia, NE China. Ore Geology Reviews, 115, 103170. doi: 10.1016/j.oregeorev.2019.103170.

Zhou JB, Wilde SA. 2013. The crustal accretion history and tectonic evolution of the NE China segment of the Central Asian Orogenic Belt. Gondwana Research, 23(4), 1365–1377. doi: 10.1016/j.gr.2012.05.012.